



Highly accessible atomically dispersed FeN_x sites coupled with $\text{Fe}_3\text{C}@\text{C}$ core-shell nanoparticles boost the oxygen catalysis for ultra-stable rechargeable Zn-air batteries

Katam Srinivas^{a,1}, Zhuo Chen^{b,1}, Fei Ma^a, Anran Chen^c, Ziheng Zhang^a, Yu Wu^a, Ming-qiang Zhu^{b,*}, Yuanfu Chen^{a,*}

^a School of Electronic Science and Engineering, and State Key Laboratory of Electronic Thin Films and Integrated Devices, University of Electronic Science and Technology of China, Chengdu 610054, China

^b College of Mechanical and Electronic Engineering, Northwest A&F University, Yangling, 712100, China

^c School of Materials and Energy, Yunnan University, Kunming 650091, China

ARTICLE INFO

Keywords:

MN_x sites
Core-shell nanoparticle
Synergistic interactions
Oxygen reduction reaction
Zn-air battery

ABSTRACT

It is significant but challenging to develop a cost-effective, high-efficiency, and stable bifunctional electrocatalyst of oxygen reduction and evolution reactions (ORR and OER) for rechargeable Zn-air batteries. Herein, we present a novel bifunctional catalyst constructed by highly accessible atomically dispersed MN_x sites coupled with core-shell nanoparticles (M-Phen-800; M = Fe, Co, and Ni) from easily accessible M-Phenanthroline (M-Phen) complexes. Due to the synergistically induced symmetric charge distribution around FeN_x sites by $\text{Fe}_3\text{C}@\text{C}$ core-shell nanoparticles, Fe-Phen-800 exhibits exceptional onset ($E_{\text{onset}} = 0.994$ V) and half-wave ($E_{1/2} = 0.878$ V) potentials for ORR and a very low overpotential of 285 mV @ 10 mA cm⁻² ($E_{j=10}$) for OER, indicating excellent bifunctional activity ($\Delta E = E_{j=10} - E_{1/2} = 0.637$ V) over the state-of-the-art Pt/C-RuO₂ (0.702 V) combination. Moreover, the Fe-Phen-800-based Zn-air battery demonstrates a remarkable energy density of 1022 Wh kg⁻¹ and greater cycling stability (>800 cycles) than the commercial Pt/C-RuO₂ battery.

1. Introduction

Rechargeable zinc-air batteries (ZABs) are one of the most promising next-generation power sources for a variety of applications due to their high theoretical energy density (1086 Wh kg⁻¹), cost-effectiveness, environmental friendliness, and excellent safety features [1–4]. Electrochemical oxygen evolution and reduction reactions (OER and ORR) are the key processes involved in metal-air batteries, but the multistep proton-coupled electron transfer taking place during these processes makes the overall system ineffective by driving the individual reactions at high overpotentials. Thankfully, the noble metal-based Pt/C (for ORR), IrO₂ and RuO₂ (for OER) electrocatalysts displayed benchmark performance. However, because of their mono-functionality, they are not suitable for metal-air battery assembly, and their inappropriate combination often results in mediocre performance [5,6]. In addition to that, the unavoidable scarcity, high cost, and poor durability hamper their large-scale implementation. Therefore, the development of highly

efficient bifunctional electrocatalysts is significant and urgent in order to alleviate the sluggish energy barrier of the electrode reactions in metal-air batteries.

To that end, considerable research efforts have been devoted toward the development of cost-effective, highly efficient, and earth-abundant nonnoble metal-based electrocatalysts [7,8]. Due to the greatly improved ORR performance and durability over commercial Pt/C, single-atom catalysts with metal-nitrogen-carbon (M-N_x-C) coordination sites have gained enormous research attention in recent years [9–11]. Among the various M-N_x-C catalysts, materials with FeN_x and CoN_x sites emerged as viable alternatives to Pt-based materials [12,13]. In general, nitrogen-rich precursors are needed to trap the metal in its atomically dispersed state (MN_x), while other heteroatoms-doping significantly boosts the catalytic performance owing to the induced charge distribution in the porous carbon network [14,15]. Specifically, zeolitic-imidazolate frameworks (ZIF) are the most widely used precursors in producing N-doped carbon, but the limited availability of

* Corresponding authors.

E-mail addresses: zmqsx@nwsuaf.edu.cn (M.-q. Zhu), yfchen@uestc.edu.cn (Y. Chen).

¹ These authors contributed equally to this work.

nitrogen-rich precursors (other than ZIF) hampers the growth of this innovative research field [16,17]. In addition to that, the multistep fabrication methods and the resulting low metal loadings (mostly ≤ 1 wt %) limit their widespread usage [18,19]. Besides that, the precursors without any heteroatoms can also be treated as a sacrificial template by pyrolyzing them in the presence of N-rich external sources (dicyandiamide, melamine, etc.) to introduce M-N_x-C sites [20]. Notably, the significance of metal size in enhancing the ORR remains unclear, and the presence of MN₄ species does not necessarily improve the electrolysis owing to the symmetric charge distribution around the metal atom. This issue can be resolved by replacing a few N-atoms of the MN₄ site with other heteroatoms, but the specific atom replacement in a material is highly complicated [21–23]. Therefore, a promising route to fabricating the bifunctional electrocatalysts would be to combine MN_x sites with nanoparticles, wherein the long-range synergistic coupling interactions between them would regulate the symmetric electronic structure of MN_x site and promote the oxygen adsorption kinetics [24–26]. Besides that, the systematic study of nanoparticle influence on either OER or ORR is still unclear when it is associated with MN_x sites, and the fabrication methods have not been generalized [27]. These issues highlight the critical need of generalized fabrication methods and point to the importance of conducting systematic research on MN_x sites and associated nanoparticle synergism.

In most cases, the amount of metal doped into the sacrificial template and the pyrolysis temperature determine the MN_x sites/atomic clusters/nanoparticles distribution in the material [28–30], and the coordinated organic ligands with the doped-metal atom play a crucial role in enhancing the ORR activity. 1,10-phenanthroline-based metal complexes (M-Phen) doped into the N-rich precursors or N-doped porous carbon has gained much attention in recent years as it provides the crucial MN_x pre-existing sites, which, upon high-temperature annealing are fixed into the N-doped carbon network and become immobilized M-N_x-C sites [31–33]. Despite the facile fabrication methods of M-Phen, their direct utilization as precursors in fabricating advanced electrocatalysts is limited, considering the high metal content that can be converted into insignificant metal nanoparticles [34,35].

To address such issues, herein we establish a facile and scalable M-Phen (M = Fe, Co, and Ni) pyrolysis method. Wherein, M-Phen was carbonized with an excess amount of dicyandiamide (DCDA; N-rich precursor) in order to trap the metal mostly in its atomic state (as MN_x). Interestingly, the carbonized M-Phen delivered densely accessible M-N_x-C sites along with graphitic layer-protected nanoparticles in a mesoporous carbon with ultrafine carbon nanotube (CNT) network. Precisely, Fe-Phen delivered the core-shell Fe₃C@C nanoparticles, while the other two delivered the carbon-shell protected metal nanoparticles along with MN_x sites. Owing to the synergistic interactions between nanoparticles and the MN_x sites on mesoporous carbon, as-prepared catalysts displayed considerable bifunctional activity (ORR and OER) to assemble Zn-air batteries. Precisely, Fe-Phen-800 exhibited better ORR performance with more positive onset ($E_{\text{onset}} = 0.994$ V) and half-wave ($E_{1/2} = 0.878$ V) potentials and required a small overpotential of 285 mV ($E_{j=10}$) to reach the current density of 10 mA cm⁻² for OER. The bifunctional activity parameter ΔE ($\Delta E = E_{j=10} - E_{1/2}$) detected for Fe-Phen-800 is 0.637 V, which is one of the best bifunctional activities detected so far and is much smaller than the Pt/C-RuO₂ combination ($\Delta E = 0.702$ V) [36]. Moreover, the Fe-Phen-800-based Zn-air battery displayed a significantly higher open-circuit potential, power density, specific capacity, and cycling stability than the commercial Pt/C-RuO₂ combination.

2. Experimental section

2.1. Synthetic approach

2.1.1. Synthesis of M(Phen)₃(NO₃)₂ complexes (denoted as M-Phen)

Transition metal-based (M = Fe, Co, and Ni) coordination complexes

(M-Phen) have been synthesized in a straightforward hydrothermal method as described. Briefly, M(Phen)₃(NO₃)₂ was prepared by dissolving 1 mmol of M(NO₃)₃·xH₂O in 6 mL of water and ethanol (2:1 vol ratio) mixture and stirring constantly at ambient temperature. To which solid 1,10-phenanthroline (3 mmol) was added and stirred for an additional 10 min to obtain a clear solution. Subsequently, the reaction mixture was transferred to a stain-less steel autoclave and hydrothermally heated at 120 °C for 6 h. After the reaction vessel cooled down to room temperature, the obtained mixture was left undisturbed for 2–3 days to obtain pure crystalline materials. The metal salts used in the synthesis of Fe-Phen, Co-Phen, and Ni-Phen are Fe(NO₃)₃·9H₂O, Co(NO₃)₂·6H₂O, and Ni(NO₃)₂·6H₂O, respectively.

2.1.2. Synthesis of M-Phen-800 catalysts

As-prepared M-Phen samples were mixed with nitrogen-rich dicyandiamide (DCDA) and manually ground for at least 5 min before being carbonized at a higher temperature. To be more specific, 300 mg of M-Phen was ground with 600 mg of DCDA (1:2 wt ratio) and then pyrolyzed in a two-step carbonization method, wherein the material was first heated at 500 °C for 1 h (heating rate of 2 °C min⁻¹) and then raised to 800 °C (5 °C min⁻¹) and heated for 2 h under flowing N₂ gas. Afterwards, the obtained black solid was treated with diluted sulfuric acid (0.5 M H₂SO₄) at 60 °C for 12 h, in order to remove the unstable metal/metal carbide species. Acid-treated samples were thoroughly washed with plenty of water and collected by centrifugation (named M-Phen-800). While extending the acid treatment for two days at 80 °C produce Fe-phen-800-H₂SO₄.

In order to have a better comparison, Fe-Phen-700 and Fe-Phen-900 were also prepared by changing the pyrolysis temperature. Besides that, the amount of DCDA used was also changed (Fe-Phen: DCDA = 1:0, 1:1, and 1:4 wt ratios) in fabricating the Fe-Phen-800-(1:0), Fe-Phen-800-(1:1), and Fe-Phen-800-(1:4) materials, in view of realizing the DCDA influence.

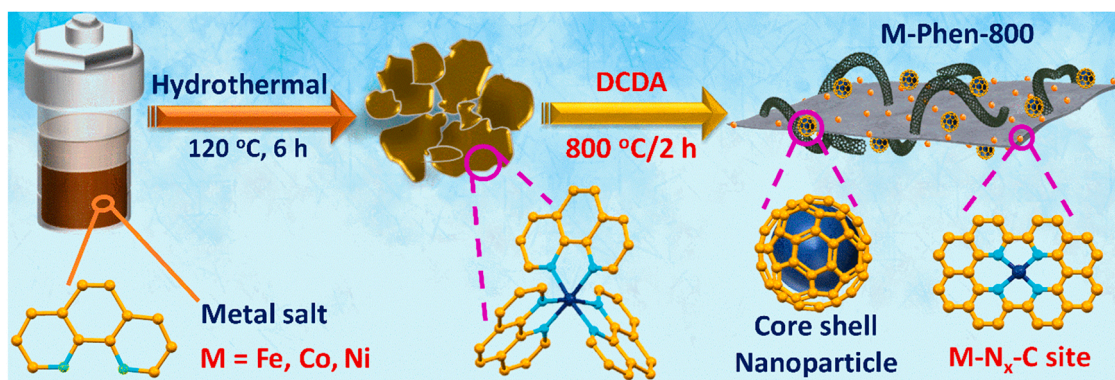
2.1.3. Materials characterization

As-prepared materials morphologies have been elucidated by Scanning electron microscopy (SEM; FEI Quanta 650 instrument at 20 kV) and the nanostructure of several key samples has been realized by Transmission electron microscopy (TEM), high-resolution TEM (HR-TEM), and high angle annular dark-field scanning TEM (HAADF-STEM). The existence of atomically dispersed MN_x sites was confirmed by aberration-corrected (AC)-HAADF-STEM analysis. Elemental distribution in the material was realized by energy dispersive spectroscopy (EDS) using a FEI Talos F200x instrument. Existing elemental compositions, their oxidation states, and the presence of MN_x sites were further confirmed by X-ray photoelectron spectroscopy (XPS; Thermo Scientific K-Alpha instrument), and the binding energy data was calibrated to 284.8 eV of C 1s spectrum. The possible crystalline phases and their diffraction patterns were evaluated by a powder X-ray diffraction study (Bruker D8 ADVANCE Cu K α -instrument). A Raman microscope with a 532 nm excitation wavelength was used in obtaining the Raman spectral data (Renishaw Corporation). The Brunauer–Emmett–Teller (BET) theory was employed in realizing the N₂ adsorption-desorption isotherms and the pore size distribution data (Quantachrome, Nova 2000e at 77 K). A description related to electrochemical measurements has been provided in the [Supporting information](#) file.

3. Results and Discussion

3.1. Synthesis and structural characterization

As schematically illustrated in [Scheme 1](#), atomically dispersed metal catalysts were fabricated by a facile hydrothermal reaction followed by a subsequent pyrolysis method. At first, nitrogen-rich metal-phenanthroline complexes (M-Phen) were prepared by treating the metal salts (Fe³⁺, Co²⁺, and Ni²⁺) with 1,10-phenanthroline in a water and ethanol



Scheme 1. Synthesis strategy of densely accessible $M-N_x-C$ sites and core-shell nanoparticles decorated mesoporous carbon.

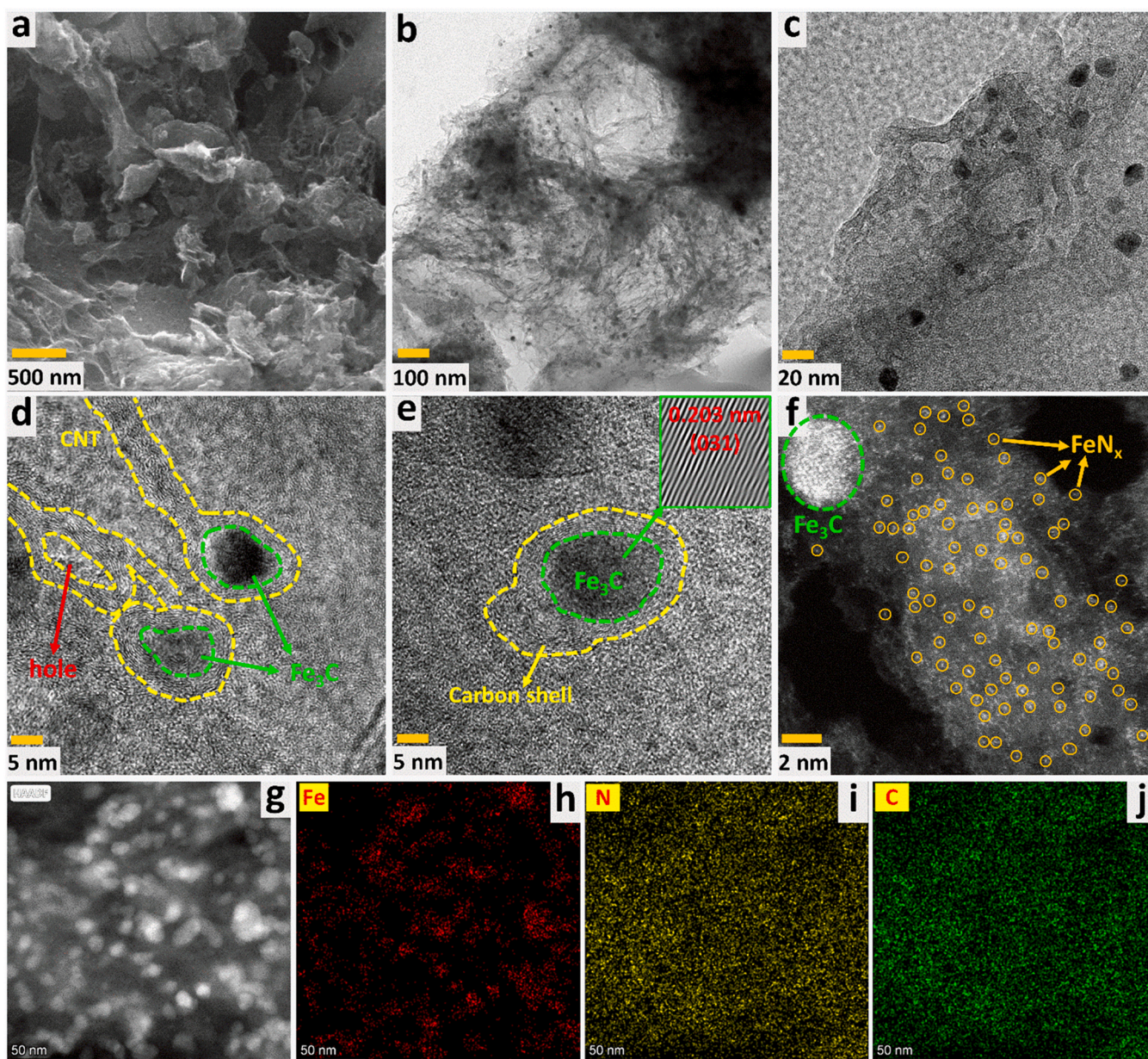


Fig. 1. (a) SEM image, (b-e) TEM and HR-TEM images, (f) AC-HAADF-STEM image, and (g-j) HAADF-STEM and EDS-mapping images of Fe-Phen-800.

mixture and adequately characterized (Fig. S1) [31]. The M-Phen coordination matrix disintegrates during high-temperature pyrolysis, resulting in an N-doped carbon matrix, in which the "N" can be found in several forms, including pyrrolic-N, pyridinic-N, and graphitic-N. But in order to trap the metal source as ORR active MN_x site, the carbon network must possess N-rich locations (mostly pyridinic-N). Keeping this in mind, an additional N-source, DCDA, has been added to M-Phen prior to high-temperature pyrolysis, resulting in M-Phen-800 with rich $M-N_x$ -C sites. In addition to incorporating more N atoms, DCDA addition also converts the derived mesoporous carbon into N-doped carbon nanotube network, which can improve electrical conductivity [37].

Notably, the irregularly shaped Fe-Phen particles were converted into a graphene-like porous network as a result of in situ-grown ultrafine carbon nanotubes upon high-temperature pyrolysis of a 1:2 wt ratio Fe-Phen-DCDA sample (Fe-Phen-800; Fig. 1a and S2). SEM images of Fe-Phen-800-(1:0), fabricated without the DCDA addition, clearly confirmed this phenomenon, as there are no CNTs and the material has a nanoflakes-like morphology with exposed Fe nanoparticles (Fig. S3). Moreover, distinct carbon nanotube growth can be observed from the SEM data of samples prepared with small and large amounts of DCDA.

To be more specific, the sample prepared with equal amounts of Fe-Phen and DCDA contained a greater number of iron carbide (FeC and $Fe_{1.88}C_{0.12}$) nanoparticles exposed within the in situ-developed CNT composite (Fe-Phen-800-(1:1); Fig. S4). While the sample fabricated with an excess amount of DCDA delivered a distinct carbon nanotube network similar to Fe-Phen-800, which can improve the electric conductivity (Fe-Phen-800-(1:4); Fig. S5). Besides that, the TEM analysis of Fe-Phen-800 confirmed the mesoporous sheet-like nanostructure composed of interconnecting ultrafine CNT network and the graphitic layer wrapped $Fe_3C@C$ nanoparticles (Fig. 1b, c and S6). The unique graphene-like nanostructure design is advantageous for improved ORR as it can provide abundant defective edge sites [38]. Precisely, a 5–7 nm wide defective carbon shell protects the (031) crystalline phased $Fe_3C@C$ nanoparticles (interplanar distance of 0.203 nm) in Fe-Phen-800, and the lattice fringes correspond to defective CNTs (interplanar distance of 0.345 nm) that are mostly broken. As a result, some of the Fe_3C nanoparticles could be removed during acid leaching, and hence there are several holes encapsulated by the carbon shell (Fig. 1d, e and S6c) [38]. Notably, the atomic dispersion of Fe on N-doped mesoporous carbon was elucidated by a potent and effective

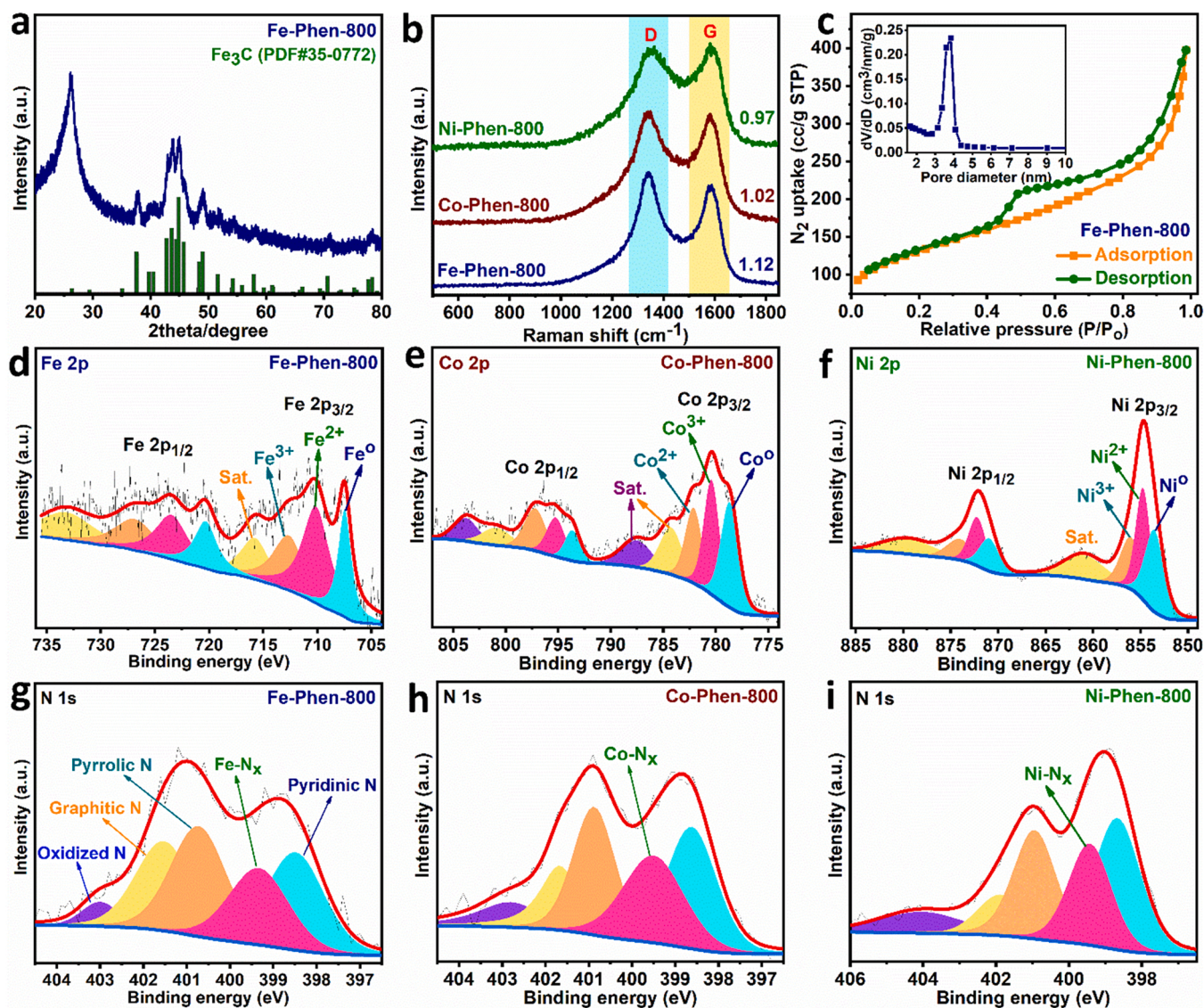


Fig. 2. (a) Powder XRD data of Fe-Phen-800, (b) Raman data of Fe-Phen-800, Co-Phen-800, and Ni-Phen-800, (c) BET surface area data of Fe-Phen-800 and its pore size distribution curve (inset), (d-f) high-resolution Fe (2p), Co (2p) and Ni (2p) XPS spectral data of M-Phen-800, and (g-i) high-resolution N (1s) XPS data of Fe-Phen-800, Co-Phen-800, and Ni-Phen-800, respectively.

aberration-corrected (AC)-HAADF-STEM analysis, which confirmed the presence of bright nanoparticles corresponding to Fe_3C and densely accessible other tiny bright spots attributed to the atomically dispersed Fe (orange circles; Fig. 1f). In addition to that, the HAADF-STEM image and the corresponding EDX-mapping images of Fe-Phen-800 confirmed the existence of nanoparticles and their uniform distribution throughout the material (Fig. 1g-j). Specifically, the homogeneous N distribution in the material suggests the ORR active FeN_x site's existence all over the carbon host.

Similar to Fe-Phen-800, the SEM image of Co-Phen-800 confirmed the sheet-like in situ-grown CNT network (Fig. S7a), and its TEM analysis additionally confirmed the ultrafine interconnecting CNT network with plenty of Co nanoparticles. Moreover, the HR-TEM analysis of Co-Phen-800 confirmed the existence of a protective graphitic layer around Co nanoparticles just like Fe-Phen-800, and there are abundant lattice defects in the material (Fig. S7). Moreover, the single atomic Co sites existence has been confirmed by AC-HAADF-STEM analysis, wherein the bright spots highlighted by orange circles confirm the CoN_x sites (Fig. S7f) [24]. While the CNT network with plenty of core-shell nanoparticles exposed composite morphology was detected for Ni-Phen-800 [39]. Additionally, the HAADF-STEM image and the corresponding EDX-mapping analysis of Ni-Phen-800 confirmed that the Ni nanoparticles are dominating in the material, which could inversely influence the ORR activity, as MN_x sites are the actual catalytic sites for ORR (Fig. S8) [28,40].

Besides that, the crystalline structure and existing phase analysis by powder XRD technique confirmed that the bright spots appearing in the Fe-Phen-800 morphology study are Fe_3C (JCPDS PDF#35-0772) nanoparticles and have not been removed during acid wash because of the protective graphitic layer (Fig. 2a) [38]. Contrarily, the powder XRD data of Fe-Phen-800-(1:0) confirmed the existence of Fe nanoparticles (JCPDS PDF#06-0696; Fig. S9a) crystalline phase instead of iron carbide phase. Therefore, it can be determined that the DCDA (formula: $\text{C}_2\text{H}_4\text{N}_4$) addition can convert the Fe nanoparticles into FeN_x sites by means of N-donation and $\text{Fe}_3\text{C}/\text{C}$ nanoparticles via C-donation. While the mixed iron carbides (FeC : JCPDS PDF#31-0619 and $\text{Co}_{12}\text{Fe}_{1.88}$: JCPDS PDF#44-1293) phase formation in equal amounts of Fe-Phen and DCDA sample (Fe-Phen-800-(1:1); Fig. S9b), additionally confirmed the C-donation. Moreover, a further increase in DCDA amount facilitates the formation of FeN_x sites and the core-shell Fe_3C nanoparticles (Fe-Phen-800-(1:4); Fig. S9c). Notably, despite using DCDA as an additional N-source, Co-Phen-800 (Co: JCPDS PDF#15-0806), and Ni-Phen-800 (Ni: JCPDS PDF#04-0850) exhibited stable metal nanoparticle crystalline phases in their XRD analysis, owing to the protective graphitic layer (Fig. S10) [24,39]. Despite the existence of metal nanoparticles, Co-Phen-800 and Ni-Phen-800 both exhibit a CNT network in their morphology study, indicating that both metal and metal carbide can catalyze CNT formation [41,42].

Moreover, the Raman spectral data of as-prepared samples displayed two prominent peaks that correspond to graphitic carbon at 1345 (D band) and 1586 cm^{-1} (G band) [43–45]. Precisely, the presence of D band signifies the defects in sp^2 hybridized hexagonal carbon network, while the G band implies the extent of graphitization. The higher I_D/I_G ratio suggests the greater possibility of structural defects as well as enhanced disorder in the graphitic carbon network [29]. Notably, the I_D/I_G value estimated for Fe-Phen-800 is considerably higher than the other samples, which means the presence of Fe atoms can better induce the formation of defective sites in order to boost the ORR catalysis (Fig. 2b) [46,47]. Evidently, the I_D/I_G value of Fe-Phen-800-(1:0) is identical to Ni-Phen-800 despite not treating with DCDA (Fig. S11).

Enhanced graphitization basically leads to an enlarged surface area, resulting in a vast number of active catalytic sites exposure. Basically, the high-temperature graphitization of a material followed by acid leaching effectively removes the unstable nanoparticles, resulting in a mesoporous carbon with plenty of hole defects and thereby achieving enhanced mass transport during ORR. Notably, all the Fe-Phen

derivatives displayed a type-IV isotherm with a hysteresis loop at a P/P_0 of 0.4–0.9 (Fig. S12), confirming the mesoporous nature [48], and the specific surface area detected was increased as the DCDA amount increased, but the pore diameter was gradually decreased from Fe-Phen-800-(1:0) to Fe-Phen-800-(1:4). Precisely, a large specific surface area of $407.38\text{ m}^2\text{ g}^{-1}$ with a distinct pore diameter of 3.84 nm was detected for Fe-Phen-800 (Fig. 2c). The mesoporous structure with a significantly higher specific surface area of Fe-Phen-800 can adequately expose the active catalytic sites, enhance electrode-electrolyte interactions, and facilitate mass transfer, all of which improve ORR activity. While changing the pyrolysis temperature significantly fine-tunes the specific surface area. Precisely, the specific surface areas detected for Fe-Phen-700 and Fe-Phen-900 are smaller than those detected for Fe-Phen-800, indicating the optimized mesoporous structure formation at 800°C pyrolysis (Fig. S13). Evidently, the Co-Phen-800 and Ni-Phen-800 also display enlarged specific surface area, but are relatively small compared to the Fe-Phen-800 (Fig. S14).

The XPS spectrum of M-Phen-800 confirms the presence of metal (Fe/Co/Ni), N, C, and O elements in the material, and the corresponding elemental data has been presented in Fig. S15. Specifically, the high-resolution Fe 2p XPS spectrum of Fe-Phen-800 displayed two major peaks (Fe $2p_{3/2}$ and $2p_{1/2}$) that are deconvoluted into three doublets, each corresponding to three different oxidation states (Fe^0 , Fe^{2+} , and Fe^{3+}) of Fe, along with shake-up satellite peaks [49–51]. The two peaks located at 707.47 and 720.30 eV can be assigned to the Fe^0 oxidation state, while the peaks situated at 710.12 and 723.46 eV are attributed to the Fe^{2+} oxidation state, and the other doublet at 712.65 and 726.86 eV belongs to the Fe^{3+} oxidation state (Fig. 2d) [52]. These findings imply that zero-valent iron (Fe^0) exists and corresponds to Fe_3C nanoparticles [27,34], while cationic $\text{Fe}^{2+/3+}$ corresponds to FeN_x coordination sites [53]. It has been demonstrated that the direct carbonization of Fe-Phen produces metallic Fe, implying that the presence of DCDA possibly stimulate the formation of Fe_3C and FeN_x as it can supply both carbon and nitrogen. Moreover, the Co 2p XPS spectrum of Co-Phen-800 displayed the typical Co $2p_{3/2}$ and $2p_{1/2}$ spin-orbit regions with Co^0 (778.67 and 783.64 eV), Co^{3+} (780.39 and 795.24 eV), and Co^{2+} (782.09 and 797.20 eV) characteristic peaks along with a pair of shake-up satellite peaks (Fig. 2e) [24,32,54]. Similarly, the Ni 2p XPS spectrum of Ni-Phen-800 displays Ni $2p_{3/2}$ and $2p_{1/2}$ spin-orbit regions with Ni^0 (853.54 and 870.94 eV), Ni^{2+} (854.72 and 872.20 eV), and Ni^{3+} (856.02 and 874.01 eV) characteristic peaks along with a shake-up doublet (Fig. 2f) [39]. The metallic peak appeared in both Co-Phen-800 and Ni-Phen-800, confirming the presence of metal nanoparticles, and the cationic metal unambiguously coordinated with pyridinic-N to form MN_x sites. Additionally, M-Phen-800 samples display a significant MN_x peak in their N 1s XPS spectra, in addition to characteristic pyridinic-N, graphitic-N, and pyrrolic-N peaks (Fig. 2g-i) [53]. Table S1 summarizes the possible deviation in peak positions of different N species of M-Phen-800 samples. ORR active pyridinic-N (25.23%), graphitic-N (22.68%), and FeN_x (20.49%) peaks are dominating in Fe-Phen-800, in addition to a significant pyrrolic-N peak (27.59%). The different types of N atoms confirm the successful N-doping into the graphitic carbon and the abundant pyrrolic-N peaks suggest topological defects such as pentagon-hexagon, pentagon-heptagon, and so on, which can also induce the catalytic performance [55]. Notably, the crucial graphitic-N content is considerably low in Co-Phen-800 (14.65%) and Ni-Phen-800 (9.98%), which can potentially influence the ORR performance (Table S2).

It is to be noted that the existing metallic content on the surface is almost the same for both Fe-Phen-800 (0.83 at%) and Co-Phen-800 (0.9 at%), while relatively high Ni content is detected on the surface of Ni-Phen-800 (2.15 at%). The XPS analysis was carried out twice to make sure the obtained results were accurate (Figs. S15–18; please see the supporting information for more details). Similarly, the SEM-based EDX elemental analysis of M-Phen-800 confirmed the existence of relatively high Ni metallic content (3.54 at%) in Ni-Phen-800, compared

to Co content (3.27 at%) in Co-Phen-800, and Fe content (2.59 at%) in Fe-Phen-800 (Figs. S19–21). Notably, abundant N content can be detected on the surface of Fe-Phen-800 (5.38 at%) and Co-Phen-800 (5.18 at%), suggesting the M-N_x sites existence, while relatively low N content in Ni-Phen-800 (7.15 at%; in terms of metal-N ratio) suggests the dominating Ni nanoparticles existence on the surface over the ORR active Ni-N_x sites. Besides, the almost similar nitrogen content detection in the EDS analysis of M-Phen-800 confirms the similar internal composition, i.e., the existence of M-N_x sites and core-shell nanoparticles. Furthermore, due to their nearly identical elemental contents, the Fe-Phen-800 and Co-Phen-800 are expected to have similar surface compositions. While the excess Ni metallic content on the Ni-Phen-800 surface, on the other hand, confirmed the dominance of metal nanoparticles over Ni-N_x sites. Moreover, the TEM-based EDX-mapping analysis of Fe-Phen-800 also confirmed the SEM-based EDX results (Fig. S22a). Moreover, the ICP-OES analysis of M-Phen-800 confirmed the considerably high metal content, which is more than most single-atom catalysts reported to date (Fig. S22b) [56,57]. What's more, the Ni metal content in Ni-Phen-800 was found to be higher compared to other samples. Furthermore, the C 1s XPS spectrum of M-Phen-800 samples exhibited three characteristic peaks corresponding to C-C, C-N, and oxidized carbon (C=O/COO) bonds, wherein the peak located at ~285.8 eV confirms the C-N bonding in supporting the M-N_x-C formation, and the highly electronegative element's connection with carbon induces the charge distribution in the material (Fig. S17). Moreover, the O 1s spectra were detected for all three samples owing to the unavoidable aerial exposure (Fig. S18), and the oxygen content was greatly improved in all these samples after preserving them for a long period of time.

3.2. Oxygen reduction reaction performance evaluation

N-doped mesoporous carbon with densely accessible M-N_x-C sites and core-shell nanoparticles is a promising candidate for both oxygen reduction and evolution reactions [17,29]. The ORR performance of

Fe-Phen-derived electrocatalysts was first evaluated in 0.1 M alkaline KOH using a rotating disk electrode (RDE). In particular, the ORR activity of Fe-based catalysts prepared with [Fe-Phen-800-(1:1), Fe-Phen-800, and Fe-Phen-800-(1:4)] and without DCDA [Fe-Phen-800-(1:0)] was measured using cyclic voltammetry (CV) followed by linear sweep voltammetry (LSV), in comparison to commercial Pt/C (20 wt%) electrocatalyst. Notably, an obvious reduction peak was detected for all of these electrocatalysts in O₂-saturated electrolyte, indicating the ability to reduce oxygen, whereas no such peak was detected in N₂-saturated electrolyte (Fig. 3a and S23). A gradual increase in CV size and the reduction peak intensity can be realized by increasing the DCDA amount (up to 1:2; Fig. 3a and S24a–25a), suggesting its influence on ORR activity. While increasing the DCDA content to 1:4 (Fig. S26a) and changing the pyrolysis temperature, the size of the CV curve was slightly reduced compared to the CV curve of Fe-Phen-800 (Figs. S29b and S30b).

The actual performance of materials was evaluated by the LSV test at a speed of 1600 rotations per minute after electrochemical activation and reduction peak detection in the CV cycling test. As can be seen in Fig. 3b, Fe-Phen-800 displayed the best onset ($E_{\text{onset}} = 0.994$ V), half-wave ($E_{1/2} = 0.878$ V) potentials, and excellent diffusion current density ($J_d = 6.78$ mA cm⁻²) compared to the other electrocatalysts, including commercial Pt/C ($E_{\text{onset}} = 0.956$ V, $E_{1/2} = 0.824$ V, and $J_d = 6.13$ mA cm⁻²). It is to be noted that the amount of DCDA added plays a key role in enhancing the diffusion limited current density. In particular, the sample fabricated without DCDA displayed the lowest J_d value, but this value increased as more DCDA was added, indicating the role of in situ-grown conductive N-doped CNTs (Figs. S24c–26c). In addition to the improved diffusion limiting current density, the ORR performance of samples was enhanced as the DCDA amount was increased (Fig. S27). Precisely, a significant improvement can be detected in $E_{1/2}$ of Fe-Phen-800 after introducing equal amounts of DCDA (Fe-Phen-800-(1:1): $E_{1/2} = 0.810$ V), compared to no DCDA addition (Fe-Phen-800-(1:0): $E_{1/2} = 0.682$ V). And it is significantly enhanced by doubling the DCDA amount (Fe-Phen-800-(1:2): $E_{1/2} = 0.878$ V). Notably, the addition of

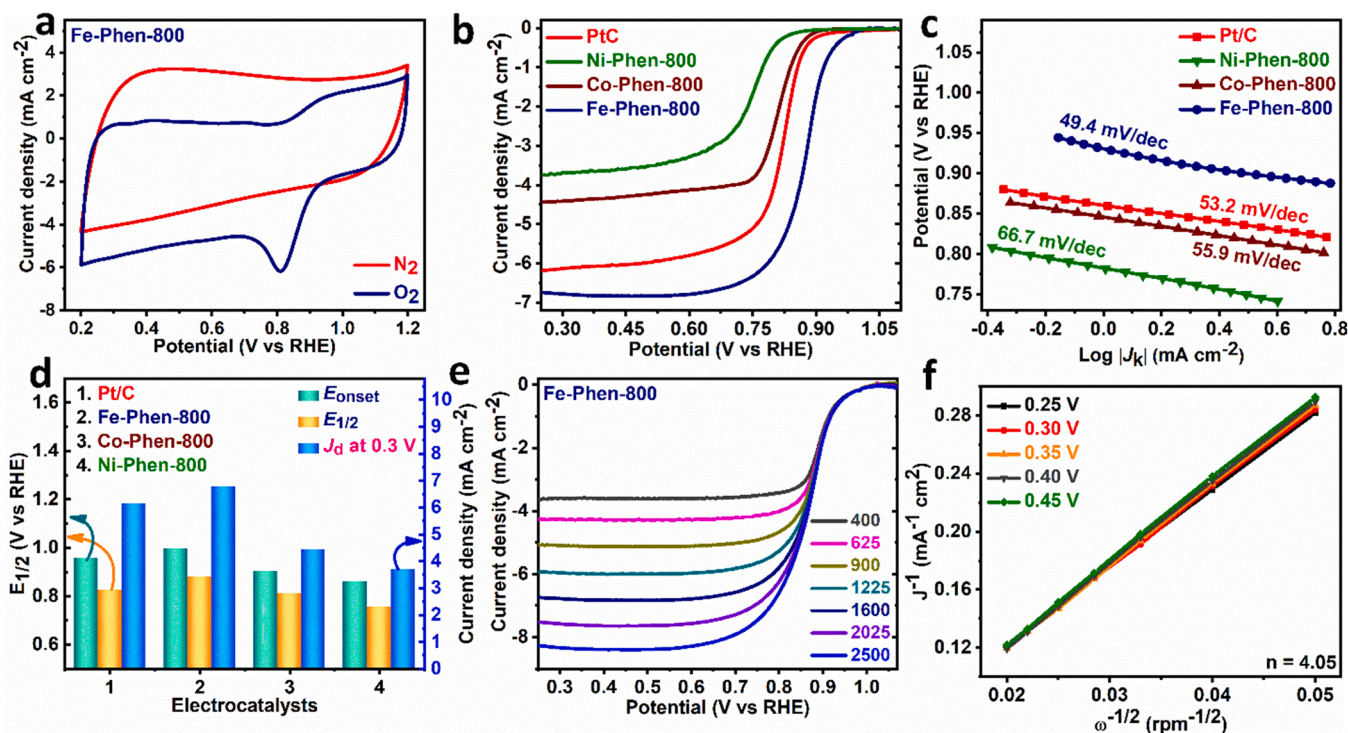


Fig. 3. (a) CV curves of Fe-Phen-800 in N₂- and O₂-saturated 0.1 M KOH solution, (b) LSV polarization curves of M-Phen-800 electrocatalysts fabricated in this study along with commercial Pt/C (20 wt%), (c) Corresponding Tafel slopes, (d) E_{onset} , $E_{1/2}$ and J_d values of electrocatalysts, (e) LSV curves of Fe-Phen-800 at different rotation speeds, and (f) K-L plots of Fe-Phen-800 derived from LSV plots obtained at different rotation speeds.

DCDA provides additional N-doping, which increases the probability of MN_x sites in the material and promotes the growth of conductive CNT. As a result, there exists improved synergistic interactions between N-doped mesoporous carbon and the single atom sites, and when there are core-shell nanoparticles, they also contribute to the overall charge distribution through the protective graphitic layer in the material [58–60]. Therefore, the symmetric charge distribution around the metal atom in the MN_x site will be regulated, which makes it more oxophilic for effective oxygen adsorption. Notably, the improved performance of samples with iron carbide nanoparticles and Fe-N_x sites confirmed the effective synergistic interactions, which were absent in the sample prepared without DCDA. However, further increase in DCDA amount resulted in poor ORR performance. Precisely, the $E_{1/2}$ of Fe-Phen-800-(1:4) was reduced to 0.806 V as a result of bulk carbon mass production during carbonization, which can possibly shadow the active sites (Fig. S27) [61].

Besides, the pioneering research efforts by Wei et al. showed that the Fe_3C nanoparticles synergistically enhance the ORR activity of single-atom FeN_x sites, and the removal of such nanoparticles results in deprived ORR performance [25]. Cui et al. demonstrated a similar phenomenon in N-doped hollow mesoporous carbon tubes containing graphitic layer-wrapped Fe_3C nanoparticles and Fe-N_x sites, demonstrating that the coexistence of both species is required for improved ORR performance. Specifically, the core-shell nanoparticles tend to promote ORR activity, and owing to the protective graphitic layer, these nanoparticles do not agglomerate to form inactive species, and, as they were located in a fixed position, they could not block the other catalytic sites [25,29]. As a result, this kind of composite material possesses abundant ORR active nanoparticles, atomically dispersed MN_x sites, and N-doped sites. Owing to the aforementioned combined structural features, as-prepared Fe-Phen-800 displayed one of the best ORR activities compared to other state-of-the-art electrocatalysts reported to date (Tables S6, and S7).

Besides, the sample prepared at a low pyrolysis temperature (Fe-Phen-700) has a low $E_{1/2}$ (0.808 V) and relatively poor diffusion current density ($J_d = 4.95 \text{ mA cm}^{-2}$) despite using the same amount of DCDA, which could be attributed to the impermeable aggregated CNT network (Fig. S29). Furthermore, the Fe-Phen-900 prepared at high temperature has more negative $E_{1/2}$ (0.795 V) and higher diffusion limited current density ($J_d = 6.62 \text{ mA cm}^{-2}$) but does not perform as well as the Fe-Phen-800, possibly due to the uneven morphology combination, i.e., a combination of nonporous aggregated CNT-composite and mesoporous CNT networks (Fig. S30). Keeping these controlled experiments (different amounts of DCDA and annealing temperature) and their influence on ORR activity in mind (Fig. S31), other metal-phenanthroline complexes were ground with double the amount of DCDA (1:2 wt ratio) and carbonized at 800 °C to obtain Co-Phen-800 and Ni-Phen-800 electrocatalysts (Fig. S32). Interestingly, the E_{onset} (0.90 V) and $E_{1/2}$ (0.81 V) detected for Co-Phen-800 are comparable with commercial Pt/C (Fig. 3b and S33), possibly owing to the Fe-Phen-800-like morphology and atomically dispersed metal species, but it displayed a relatively low J_d (4.41 mA cm^{-2}), indicating that J_d is affected not only by the amount of DCDA present but also by the metallic species present. In contrast, Ni-Phen-800 performed poorly in ORR evaluation ($E_{\text{onset}} = 0.86 \text{ V}$, $E_{1/2} = 0.753 \text{ V}$, and $J_d = 3.68 \text{ mA cm}^{-2}$), possibly owing to the surface predominance of Ni nanoparticles over NiN_x sites, confirming the significance of Fe- and Co-based electrocatalysts in ORR catalysis.

Furthermore, due to the involved proton-coupled multi-electron transfer mechanism, most of the ORR electrocatalysts display considerably high thermodynamic barriers, resulting in high Tafel slopes, which actually describe the feasibility of a reaction [62]. Because the Tafel slope value represents the feasibility of a reaction, an ideal electrocatalyst must have a lower Tafel slope. Among the electrocatalysts fabricated in this study, the Fe-Phen-800 presented the smallest Tafel slope (49.4 mV dec^{-1} ; Fig. 3c), while the Co-Phen-800 (55.9 mV dec^{-1}) showed reaction kinetics comparable to Pt/C (53.2 mV dec^{-1}). Fig. 3d,

summarizes the E_{onset} , $E_{1/2}$, and J_d values of electrocatalysts. In general, ORR involves two or four electron transfer mechanisms. Therefore, calculating the number of electrons transferred during the ORR process is essential. In order to estimate the number of electrons transferred (n) during ORR, Fe-Phen-800 was subjected to LSV operation at different rotation rates, ranging from 400 to 2500 rpm (Fig. 3e), and then the Koutecky–Levich (K–L) equation was used to calculate the ' n ' value. As shown in Fig. 3f, the number of electrons transferred is 4.05 for Fe-Phen-800, whereas Co-Phen-800 has a slightly lower value ($n = 3.85$) and Ni-Phen-800 has even lower selectivity, with a ' n ' value as low as 3.25 (Fig. S34). Furthermore, the Fe-based control samples with varying amounts of DCDA (Figs. S24d–26d) and annealing temperatures (Figs. S29d, and S30d) showed an ' n ' value close to 4, indicating a four-electron transfer mechanism. In addition to that, a rotating ring-disk electrode (RRDE) experiment was carried out to confirm the ' n ' value during ORR and also to estimate the yield of hydrogen peroxide (H_2O_2). As shown in Fig. 4a, M-Phen-800 catalysts have a ' n ' value similar to Pt/C ($n \sim 4$) and produce negligible H_2O_2 , indicating that the ORR occurs via a 4-electron transfer mechanism. In addition to its poor ORR performance, Ni-Phen-800 has a low ' n ' value and a high H_2O_2 yield, supporting the data obtained by the RRDE experiment [32].

In order to understand the accessible surface area at the electrode-electrolyte interface, it is necessary to estimate the electrochemically active surface area (ECSA) of electrocatalysts in addition to the specific surface area detection by BET analysis. ECSA can be obtained from the double-layer capacitance (C_{dl}) values estimated from the CV cycling tests operated in the non-Faradic capacitive current range (Figs. S35–37). Besides having large BET surface areas, M-Phen-800 catalysts also showed excellent C_{dl} values compared to most recently reported electrocatalysts. Precisely, Fe-Phen-800 exhibits the highest ECSA (Fig. 4b), compared to Co-Phen-800 and Ni-Phen-800, displaying a largely accessible active surface area that can expose abundant active catalytic sites, which is consistent with its BET data (Table S3). As can be seen in Table S4, increased DCDA content increased the BET surface area and the ECSA of samples from Fe-Phen-800-(1:0) to Fe-Phen-800-(1:2). Despite the improved specific surface area, excess addition of DCDA does not improve the ECSA, possibly owing to the buried active sites in the carbon bulk of Fe-Phen-800-(1:4) [61]. Besides, the change in temperature does not improve the electrochemically active surface area and is consistent with the BET data (Table S5 and Figs. S13, S36).

Moreover, in view of understanding the impact for $\text{Fe}_3\text{C}@C$ nanoparticles on ORR activity of FeN_x sites, Fe-Phen-800 was extensively treated with H_2SO_4 solution at 80 °C temperature and obtained the Fe-Phen-800- H_2SO_4 [38]. The powder XRD data of Fe-Phen-800- H_2SO_4 displays only two diffraction peaks that correspond to the graphitic carbon alone, and the diffraction peaks that correspond to $\text{Fe}_3\text{C}@C$ nanoparticles have completely disappeared (Fig. S38). While the metallic content was extensively decreased in the XPS survey spectrum, confirming the successful removal of nanoparticles. Evidently, the ORR active Fe-N_x and pyridinic-N sites content was significantly increased in Fe-Phen-800- H_2SO_4 (Fig. S39b). Notably, the half-wave potential of Fe-Phen-800- H_2SO_4 was reduced by 73 mV compared to its Fe-Phen-800 counterpart (Fig. S39d). The inferior ORR activity of Fe-Phen-800- H_2SO_4 with FeN_x sites alone suggests that the $\text{Fe}_3\text{C}@C$ nanoparticles are essential for enhancing the ORR activity [25]. Therefore, it can be concluded that the $\text{Fe}_3\text{C}@C$ nanoparticles and the atomically dispersed FeN_x sites must coexist to achieve the best ORR performance. Recent investigation by Jiang et al. established that the catalysts with both FeN_x sites and $\text{Fe}/\text{Fe}_3\text{C}$ nanocrystals demonstrated high ORR activity, and the DFT calculations corroborated that the existing Fe nanoparticles synergistically facilitate the O_2 adsorption kinetics of FeN_x sites [63]. Therefore, considering the control sample ORR activity and the previously published single-atom catalysts with associated Fe_3C nanoparticle studies, it can be reasonably postulated that the $\text{Fe}_3\text{C}@C$ nanoparticles synergistically modulating the surface structure of FeN_x sites in Fe-Phen-800 and thereby improving the oxygen

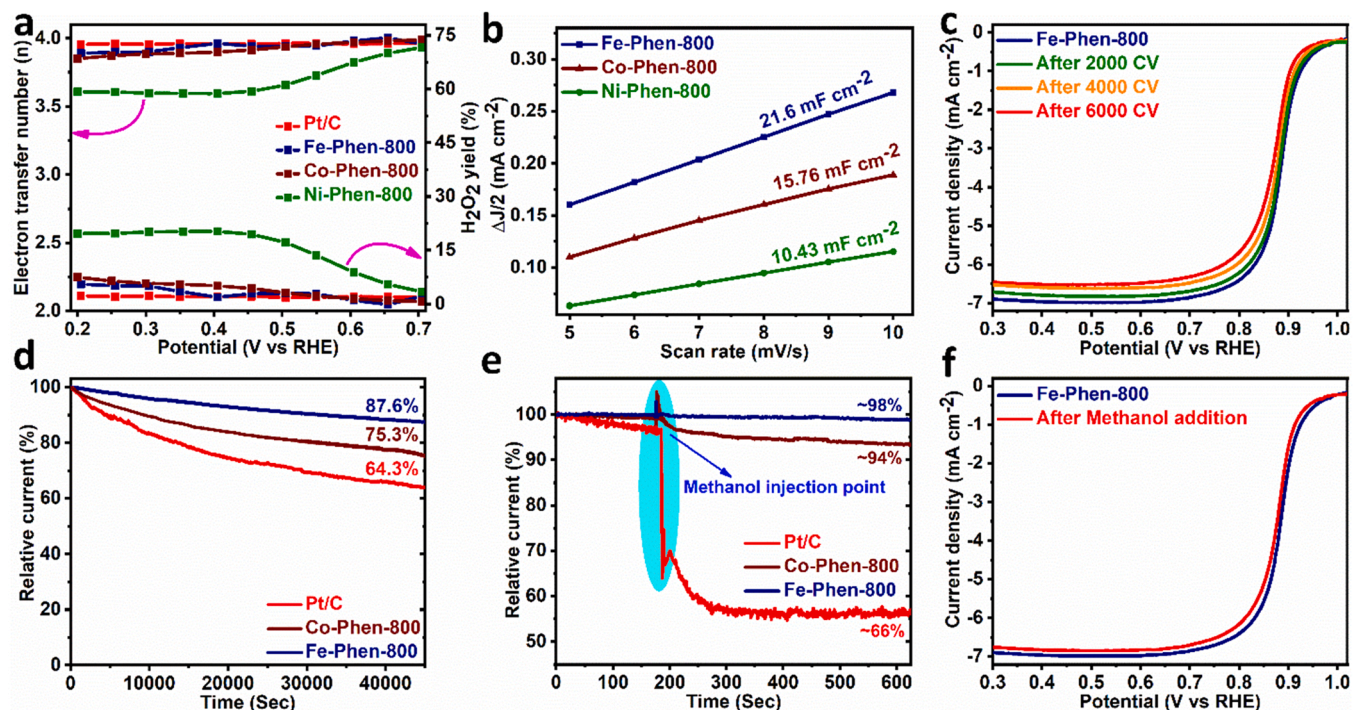


Fig. 4. (a) Electron transfer number and H₂O₂ yields of M-Phen-800, and Pt/C catalysts, (b) ECSA data of electrocatalysts obtained from CV cycling test, (c) LSV curves of Fe-Phen-800 before and after 6000 continuous CV cycles, (d) chronoamperometric *i-t* test data of Fe-Phen-800, Co-Phen-800 and Pt/C, (e) chronoamperometric *i-t* test data of Fe-Phen-800, Co-Phen-800, and Pt/C after adding 10 mL of methanol to 90 mL of 0.1 M KOH electrolyte, and (f) LSV curves of Fe-Phen-800 before and after adding methanol.

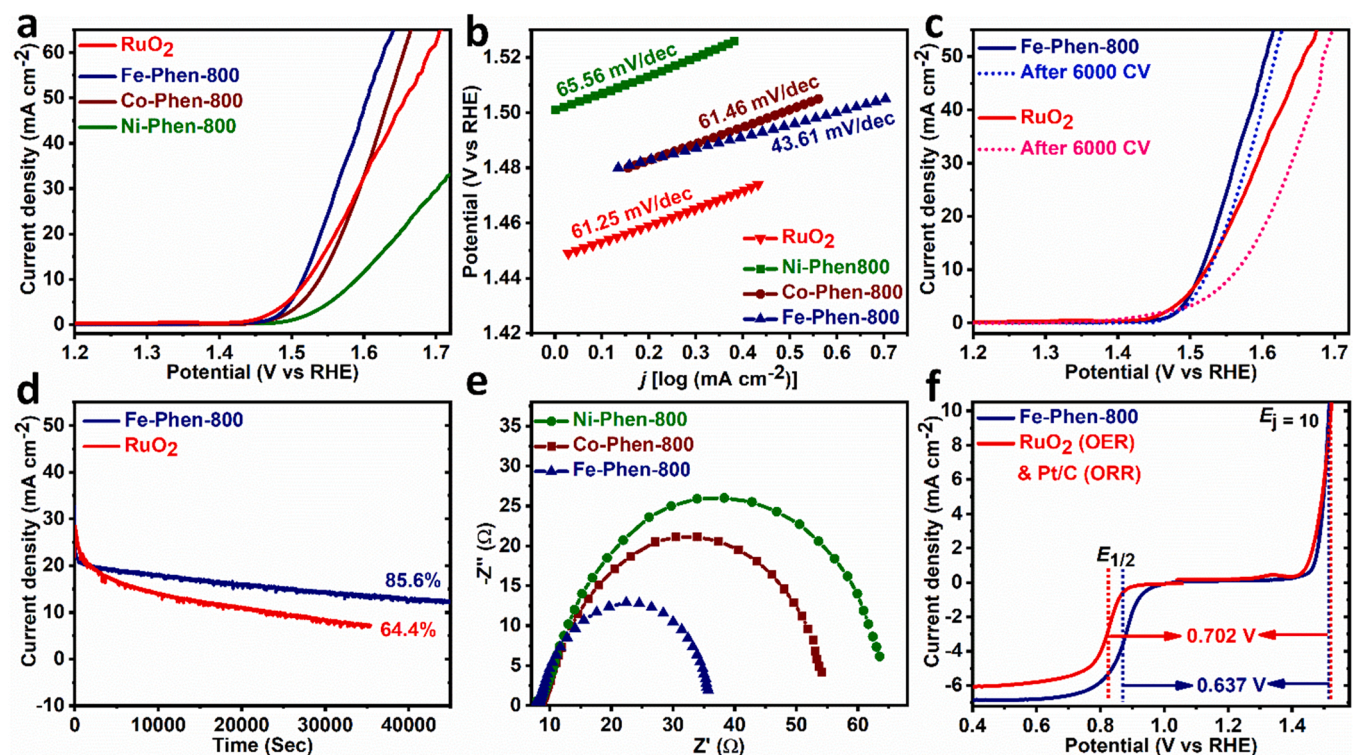


Fig. 5. (a) OER LSV polarization curves of M-Phen-800 and RuO₂ catalyst, (b) Corresponding Tafel slopes, (c) LSV curves of Fe-Phen-800 and RuO₂ before and after 6000 continuous CV cycles, (d) chronoamperometric *i-t* test data of Fe-Phen-800, and RuO₂ at 20 mA cm⁻² current density, (e) Nyquist plots of Fe-Phen-800, Co-Phen-800 and Ni-Phen-800 catalysts at an overpotential of 285 mV, and (f) LSV overall curves for ORR and OER including the voltage gap (ΔE) between E_{1/2} for ORR and E_{j=10} for OER.

adsorption kinetics to display exceptional ORR activity.

Moreover, the electrocatalyst's durability in harsh electrolytes is one of the crucial parameters in real-world implementation, as Pt/C is sensitive to long-term operations. At first, Fe-Phen-800 was subjected to a continuous CV cycling (6000 CV cycles) test. Fig. 4c,d show that Fe-Phen-800 has a small change in $E_{1/2}$ ($\Delta E_{1/2} = 14$ mV) after long-time cycling tests, and a small decay in relative current (12.4%) was detected after overnight chronoamperometric i - t test (at 0.6 V with 1600 rpm), indicating excellent durability. While Co-Phen-800 retains 75.3% of the relative current and Pt/C can barely retain 64.3%, indicating the M-Phen-800 electrocatalysts superiority in long-time operations. Besides that, tolerance towards methanol addition is an important phenomenon in fuel cell applications, as the Pt/C electrocatalyst is extremely sensitive to methanol addition (Fig. 4e). Interestingly, the LSV curve obtained for Fe-Phen-800 after methanol addition deviates slightly from its initial curve ($\Delta E_{1/2} = 8$ mV; Fig. 4f), while the chronoamperometric i - t test shows almost no change. Notably, the i - t test of Pt/C after methanol addition shows approximately 34% relative current decay (cliff-like current drop; Fig. 4e), demonstrating its sensitivity, while Co-Phen-800 exhibits excellent tolerance to methanol addition and also displays remarkable cycling stability (Fig. S40).

3.3. Oxygen evolution reaction performance evaluation

In addition to excellent ORR activity, M-Phen-800 samples displayed considerable OER activity in a 1.0 M KOH electrolyte [13,64,65]. As can be seen in Fig. 5a, Fe-Phen-800 showed the best OER performance compared to the other control samples and is better than the commercial RuO₂ catalyst. Precisely, 285 mV overpotential is required for Fe-Phen-800 to reach the benchmark current density of 10 mA cm⁻² ($E_{j=10}$), surpassing the Co-Phen-800 ($E_{j=10} = 308$ mV) and the Ni-Phen-800 ($E_{j=10} = 360$ mV). Despite comparable OER activity at lower current density, Fe-Phen-800 outperforms the state-of-the-art RuO₂ ($E_{j=10} = 293$ mV) at above 10 mA cm⁻², confirming its exceptional bifunctional activity. In addition to that, the Tafel slopes derived from corresponding LSV plots confirmed the smaller electron and mass transfer barriers with enhanced OER kinetics for Fe-Phen-800 (43.61 mV dec⁻¹) over the other electrocatalysts studied herewith (Fig. 5b).

Besides the excellent OER activity, the catalytic stability of Fe-Phen-800 was also estimated by conducting CV cycling for a continuous 6000 cycles (Fig. 5c), wherein the obtained LSV plot after the OER cycling test is almost comparable with the initial one ($\Delta E_{j=10} = 11$ mV), while a large deviation in OER activity is detected for RuO₂ after the CV cycling test ($\Delta E_{j=10} = 39$ mV) [58]. Additionally, the chronoamperometric i - t test conducted at 20 mA cm⁻² current density for both Fe-Phen-800 and RuO₂ confirmed the newly fabricated samples better durability in harsh alkaline medium (Fig. 5d) [50]. Moreover, the electrochemical impedance spectroscopy (EIS) technique was employed on all these electrocatalysts in order to estimate the interactions at the electrode-electrolyte interface. As shown in Fig. 5e, Fe-Phen-800 (27.93 Ω) displayed the smallest charge transfer resistance compared to Co-Phen-800 (36.15 Ω) and Ni-Phen-800 (45.59 Ω) [66,67]. In addition, the key bifunctional activity of a material can be estimated by determining the potential gap between OER and ORR ($\Delta E = E_{j=10} - E_{1/2}$). In general, a smaller ΔE indicates better bifunctional activity. Because of the state-of-the-art OER and ORR activities, Fe-Phen-800 owned the smallest potential gap (ΔE) of 0.637 V, which is significantly smaller than the Co-Phen-800 (0.728 V), Ni-Phen-800 (0.837 V), and commercial Pt/C-RuO₂ combination (0.702 V) (Fig. 5f and S41). Moreover, the ΔE detected for Fe-Phen-800 is one of the best bifunctional activities detected and is better than most of the reported bifunctional electrocatalysts (Table S7) [36,68]. Recent pioneering research efforts have established that the M-N_x-C site serves as the active catalytic site in pure single-atom catalysts for both OER and ORR [48,69]. Similarly, materials containing Fe₃C nanoparticles alone can exhibit significant bifunctional activity

[70]. Contrarily, in the case of single-atom catalysts associated with nanosized metal or metal carbide, the M-N_x-C site was acknowledged as the ORR active site, and the nanosized metal or metal carbide was considered the OER active site [8]. While some studies revealed that the core-shell nanoparticles cannot contact the reactants as they are wrapped by a graphite layer and hence cannot be treated as direct active sites [71], instead they can induce the charge distribution in the surrounding carbon network in order to modulate the surface structure of M-N_x-C sites [25]. Therefore, considering the above facts, Fe₃C@C nanoparticle-assisted Fe-N_x sites were considered the active catalytic sites for both OER and ORR. Wherein the former acts as the electronic structure modulator by means of long-range synergistic coupling interactions, and the latter directly participates in the reaction mechanism. However, much more in-depth theoretical and experimental support is necessary to confirm the real active sites for both OER and ORR.

3.4. Zinc-Air battery performance evaluation

Zinc-air batteries (ZABs) are the most intriguing alternatives to lithium-ion technology for future energy storage [3,4,72]. ZABs have been around for 100 years, and the primary ZAB was first introduced to the market in 1932 with buoys and hearing aid-type telecommunication applications [73–75]. However, rechargeable ZABs were commercialized in 2012 by NantEnergy Corporation with a meager energy density of 35 Wh kg⁻¹ [4]. The problem that arises in ZABs is that the air cathode must exhibit significant bifunctional activity (ORR and OER). Owing to the multistep proton-coupled electron transfer mechanisms of both ORR and OER, the assembled ZABs are not able to fulfill the real-world requirements [76–79]. In general, material with excellent ORR does not necessarily display significant OER. For example, Pt-based catalysts show excellent ORR but are lousy for OER. In that case, these materials must be combined with OER active materials, but this kind of mixing often results in mediocre performance [5,6]. Similar air electrodes with a combination of Ag, Co, WC, and NiS on carbon were first developed by Westinghouse Electric Corporation [80,81], wherein Ag stabilized NiS promoting the ORR, and Co promoted the OER [82]. Despite different materials usage in ZABs fabrication [83,84], single-atom catalysts with exceptional ORR activity and decent OER performance have received much research significance as air electrodes recently [85].

Considering the facile and scalable synthetic approach to a wide variety of transition metals and their exceptional performance towards ORR and OER activity, the as-obtained Fe-Phen-800 was used as a cathode material in assembling the rechargeable ZAB in order to realize its practical application [86]. A lab made ZAB was assembled by Fe-Phen-800 cathode and zinc plate anode in 6 M KOH + 0.02 M Zn (OAc)₂ aqueous electrolyte (Fig. 6a) [78]. Due to the considerably diminished reaction kinetics, Fe-Phen-800-based ZAB demonstrated a significantly higher open circuit voltage of 1.492 V, surpassing the commercial Pt/C-RuO₂ battery (1.423 V), and being comparable to the majority of the state-of-the-art electrocatalysts reported recently (Fig. 6b).

Moreover, the rate performance detected for both the assembled ZABs at different current densities confirmed that the Fe-Phen-800 ZAB is significantly better than the Pt/C-RuO₂ combination. Precisely, Fe-Phen-800-based ZAB delivers the high voltages of 1.380, 1.364, 1.355, and 1.317 V at current densities of 1, 5, 10, and 50 mA cm⁻², respectively, and Pt/C-based ZAB delivers the voltages of 1.368, 1.333, 1.315, and 1.220 V at the same current densities (Fig. 6c). Although similar voltages are detected at smaller current densities for both ZABs, the deviation becomes significant at higher current densities, suggesting the better rate performance of Fe-Phen-800. Notably, a 1.7-fold higher power density is acquired by the Fe-Phen-800 battery (222.63 mW cm⁻² at maximum; Fig. 6d) over the commercial Pt/C-RuO₂ battery (130.1 mW cm⁻² at maximum) [27,29], and it exhibited a large specific

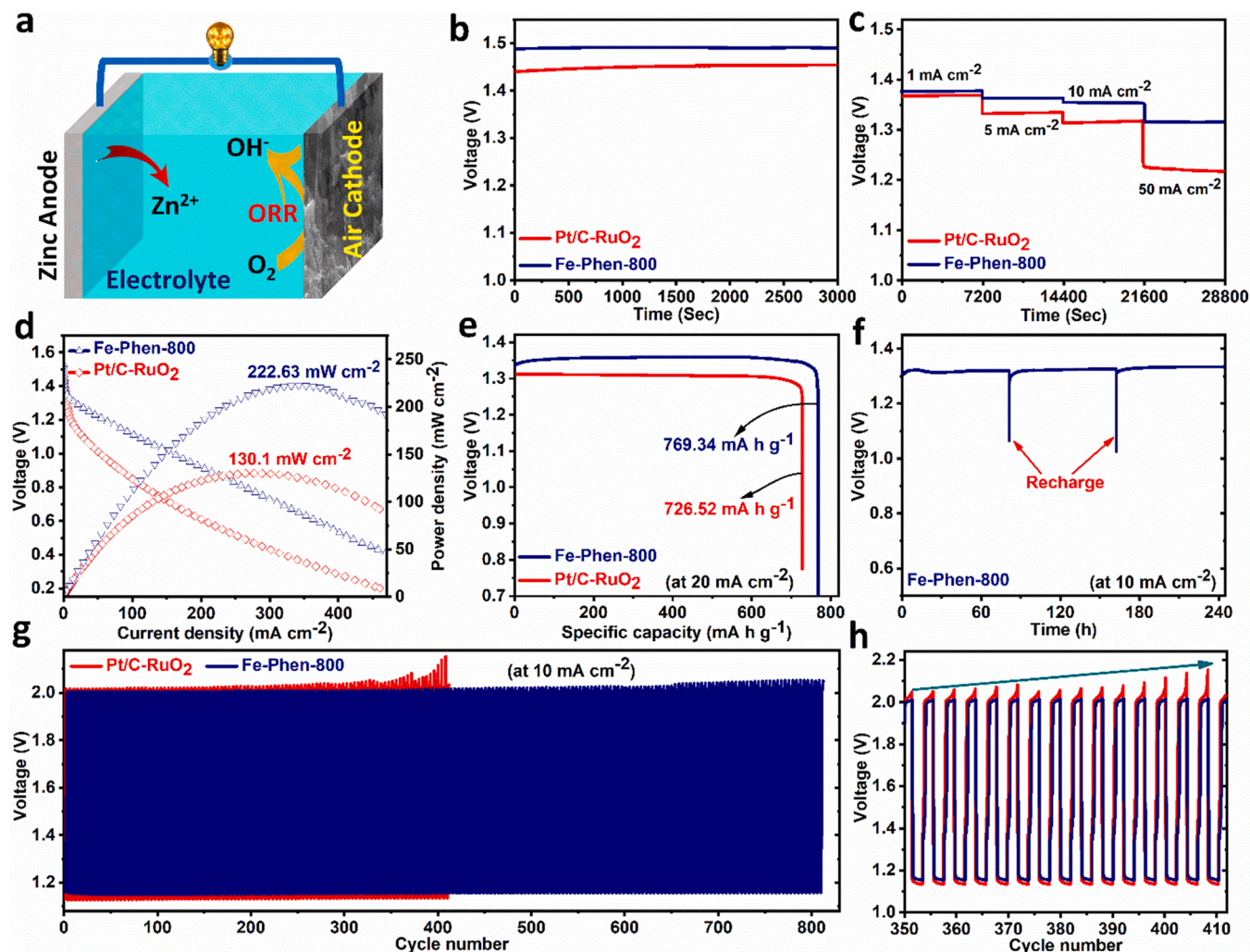


Fig. 6. (a) schematic configuration of the assembled Zn–air battery, (b) Open-circuit plots, (c) rate performances at different current densities, (d) Polarization and power density curves, (e) long-time galvanostatic discharge curve of a Zn–air battery with Fe-Phen-800 and Pt/C-RuO₂ as cathode catalysts until complete consumption of Zn anode at 20 mA cm⁻², (f) Fe-Phen-800 ZAB recharging performance test by refueling the electrolyte and the Zn anode, (g) cycling stability of zinc–air flow batteries with Fe-Phen-800 or Pt/C-RuO₂ as air cathode, and (h) zoomed-in view of charge/discharge plots at around 400 cycles.

discharge capacity of 769.34 mA h g⁻¹ (estimated based on the consumed Zn weight; Fig. 6e) over the Pt/C-RuO₂ battery (726.52 mA h g⁻¹), indicating the best ORR efficiency [86]. Additionally, the achieved specific energy density for Fe-Phen-800 (1022 Wh kg⁻¹) is one of the best when compared to the state-of-the-art electrocatalysts [4,11,86]. Notably, the Fe-Phen-800 battery is mechanically rechargeable by refueling the electrolyte and the zinc anode; however, the voltage detected is almost the same after a long period of operation, indicating its exceptional performance (Fig. 6f) [27,87].

Besides, the cycling stability of Fe-Phen-800 and Pt/C-RuO₂ cathodes was estimated by a continuous galvanostatic discharge-charge cycling test at 10 mA cm⁻² with a 200 s per cycle duration (Fig. 6g). Impressively, the voltage profile of a cell assembled by Fe-Phen-800 displayed less variation with excellent rechargeability than the other one. In addition to that, a smaller overpotential (voltage gap of 0.857 V) was noticed for the Fe-Phen-800 battery with an exceptional round-trip efficiency of 57.64% and was slightly dropped after continuous 800 discharge-charge cycles (56.24 % with 0.896 V overpotential requirement; Fig. S42) [62]. While under the same set of conditions, Pt/C-RuO₂ battery displays exceptional round-trip efficiency of 64.64 % with a small overpotential (0.698 V) requirement but is sharply increased to 0.829 V overpotential within several discharge-charge cycles

(round-trip efficiency drops to 55.76 %), and it shows 52.63 % round-trip efficiency after 400 cycles with overpotential as high as 1.01 V, but after the same number of cycles Fe-Phen-800 battery displays a much higher round-trip efficiency of 57.27 % (Fig. 6h and S42). The significant catalytic performance of non-noble metal-based Fe-Phen-800 over the commercial Pt/C catalyst and the other state-of-the-art catalysts, together with the facile and generalized large-scale fabrication strategy, pave the path for developing many more cost-effective and highly efficient electrocatalysts toward the commercialization of metal-air batteries.

4. Conclusions

In conclusion, we have established a cost-effective and highly efficient strategy for bifunctional electrocatalyst fabrication via a facile hydrothermal reaction and high-temperature pyrolysis method. Following this methodology, Fe, Co, and Ni-based composite (M-Phen-800) catalysts have been synthesized, and this novel strategy can be extended to a variety of transition metals in fabricating advanced electrocatalysts for clean energy technologies. Owing to the synergistic interactions between isolated core-shell nanoparticles and the atomically dispersed MN_x sites within a N-doped mesoporous carbon, together with improved conductivity of ultrafine CNT network, M-Phen-800 samples

displayed exceptional bifunctional (OER and ORR) activity. Owing to the protective graphitic layer, the associated nanoparticles stimulate the electron/mass transport through the carbon network, which can effectively modulate the charge distribution around the M-N_x-C sites and thereby deliver exceptional activity in both half cells of the assembled Zn-air battery. Specifically, Fe-Phen-800 displayed significantly better ORR performance than commercial Pt/C, with much better onset (0.994 V), half-wave potentials (0.878 V), and high limiting current density (6.78 mA cm⁻²). The Fe-Phen-800-based zinc-air battery demonstrated a high and stable open circuit potential (1.495 V), a high peak power density (222.63 mW cm⁻²), a remarkable specific capacity (769.34 mA h g⁻¹), and exceptional discharge-charge cycling stability (800 cycles) under practical battery operating conditions. Therefore, it is believed that the novel and adoptable synthesis strategy reported herewith can open up a new avenue in designing and fabricating advanced electrocatalysts for future energy technologies.

CRediT authorship contribution statement

Katam Srinivas: Conceptualization, Methodology, Investigation, Formal analysis, Visualization, Writing-original draft. **Zhuo Chen:** Investigation, Formal analysis, Validation, Visualization. **Fei Ma:** Software, Data curation, Formal analysis. **Anran Chen:** Resources, Software, Formal analysis. **Ziheng Zhang:** Data curation, Formal analysis. **Yu Wu:** Data curation, Validation, Visualization. **Ming-qiang Zhu:** Resources, Software, Formal analysis. **Yuanfu Chen:** Conceptualization, Supervision, Funding acquisition, Project administration, Resources, Writing-review and editing.

Declaration of Competing Interest

The authors declare that they have no known competing financial interests or personal relationships that could have appeared to influence the work reported in this paper.

Data availability

No data was used for the research described in the article.

Acknowledgments

The research was financially supported by the National Natural Science Foundation of China (Grant No. 21773024), Natural Science Foundation of Sichuan Province of China (Grant No. 2023NSFC0084), and China Postdoctoral Science Foundation (Grant No. 2019M663469).

Appendix A. Supporting information

Supplementary data associated with this article can be found in the online version at [doi:10.1016/j.apcatb.2023.122887](https://doi.org/10.1016/j.apcatb.2023.122887).

References

- Z. Zhao, X. Fan, J. Ding, W. Hu, C. Zhong, J. Lu, Challenges in zinc electrodes for alkaline zinc-air batteries: obstacles to commercialization, *ACS Energy Lett.* 4 (2019) 2259–2270, <https://doi.org/10.1021/acseenergylett.9b01541>.
- Y. Wang, J. Liu, T. Lu, R. He, N. Xu, J. Qiao, Ultra-high voltage efficiency rechargeable zinc-air battery based on high-performance structurally regulated metal-rich nickel phosphides and carbon hybrids bifunctional electrocatalysts, *Appl. Catal. B Environ.* 321 (2023), 122041, <https://doi.org/10.1016/j.apcatb.2022.122041>.
- Y. Li, H. Dai, Recent advances in zinc-air batteries, *Chem. Soc. Rev.* 43 (2014) 5257–5275, <https://doi.org/10.1039/C4CS00015C>.
- J. Zhang, Q. Zhou, Y. Tang, L. Zhang, Y. Li, Zinc-air batteries: are they ready for prime time? *Chem. Sci.* 10 (2019) 8924–8929, <https://doi.org/10.1039/C9SC04221K>.
- T. Liu, J. Mou, Z. Wu, C. Lv, J. Huang, M. Liu, A facile and scalable strategy for fabrication of superior bifunctional freestanding air electrodes for flexible zinc-air batteries, *Adv. Funct. Mater.* 30 (2020), 2003407, <https://doi.org/10.1002/adfm.202003407>.
- Y. Tan, Z. Zhang, Z. Lei, L. Yu, W. Wu, Z. Wang, N. Cheng, Electronic modulation optimizes OH⁻ intermediate adsorption on Co-N_x-C sites via coupling CoNi alloy in hollow carbon nanopolyhedron toward efficient reversible oxygen electrocatalysis, *Appl. Catal. B Environ.* 304 (2022), 121006, <https://doi.org/10.1016/j.apcatb.2021.121006>.
- Y. Qu, Z. Li, W. Chen, Y. Lin, T. Yuan, Z. Yang, C. Zhao, J. Wang, C. Zhao, X. Wang, F. Zhou, Z. Zhuang, Y. Wu, Y. Li, Direct transformation of bulk copper into copper single sites via emitting and trapping of atoms, *Nat. Catal.* 1 (2018) 781–786, <https://doi.org/10.1038/s41929-018-0146-x>.
- J. Li, Y. Meng, L. Zhang, G. Li, Z. Shi, P. Hou, C. Liu, H. Cheng, M. Shao, Dual-phasic carbon with Co single atoms and nanoparticles as a bifunctional oxygen electrocatalyst for rechargeable Zn-air batteries, *Adv. Funct. Mater.* 31 (2021), 2103360, <https://doi.org/10.1002/adfm.202103360>.
- W. Chen, J. Pei, C.-T. He, J. Wan, H. Ren, Y. Wang, J. Dong, K. Wu, W.-C. Cheong, J. Mao, X. Zheng, W. Yan, Z. Zhuang, C. Chen, Q. Peng, D. Wang, Y. Li, Single tungsten atoms supported on MOF-derived N-doped carbon for robust electrochemical hydrogen evolution, *Adv. Mater.* 30 (2018), 1800396, <https://doi.org/10.1002/adma.201800396>.
- J. Li, M. Chen, D.A. Cullen, S. Hwang, M. Wang, B. Li, K. Liu, S. Karakalos, M. Lucero, H. Zhang, C. Lei, H. Xu, G.E. Sterbinsky, Z. Feng, D. Su, K.L. More, G. Wang, Z. Wang, G. Wu, Atomically dispersed manganese catalysts for oxygen reduction in proton-exchange membrane fuel cells, *Nat. Catal.* 1 (2018) 935–945, <https://doi.org/10.1038/s41929-018-0164-8>.
- Y. Wang, H. Su, Y. He, L. Li, S. Zhu, H. Shen, P. Xie, X. Fu, G. Zhou, C. Feng, D. Zhao, F. Xiao, X. Zhu, Y. Zeng, M. Shao, S. Chen, G. Wu, J. Zeng, C. Wang, Advanced electrocatalysts with single-metal-atom active sites, *Chem. Rev.* 120 (2020) 12217–12314, <https://doi.org/10.1021/acs.chemrev.0c00594>.
- M. Zhao, F. Xiao, H. Zhang, W. Chen, H. Sun, Z. Wang, B. Zhang, L. Song, Y. Yang, C. Ma, Y. Han, W. Huang, A pH-universal ORR catalyst with single-atom iron sites derived from a double-layer MOF for superior flexible quasi-solid-state rechargeable Zn-air batteries, *Energy Environ. Sci.* 14 (2021) 6455–6463, <https://doi.org/10.1039/D1EE01602D>.
- J. Sun, P. Peng, Y. Xie, X. Yu, K. Qu, L. Feng, H. Bao, F. Luo, Z. Yang, Co single atoms and Co nanoparticle relay electrocatalyst for rechargeable zinc air batteries, *Appl. Catal. B Environ.* 319 (2022), 121905, <https://doi.org/10.1016/j.apcatb.2022.121905>.
- Y. Wang, N. Xu, R. He, L. Peng, D. Cai, J. Qiao, Large-scale defect-engineering tailored tri-doped graphene as a metal-free bifunctional catalyst for superior electrocatalytic oxygen reaction in rechargeable Zn-air battery, *Appl. Catal. B Environ.* 285 (2021), 119811, <https://doi.org/10.1016/j.apcatb.2020.119811>.
- H. Jin, X. Zhao, L. Liang, P. Ji, B. Liu, C. Hu, D. He, S. Mu, Sulfate ions induced concave porous S-N Co-doped carbon confined Fe_N₄ nanoclusters with Fe-N₄ sites for efficient oxygen reduction in alkaline and acid media, *Small* 17 (2021), 2101001, <https://doi.org/10.1002/sml.202101001>.
- X. Gong, J. Zhu, J. Li, R. Gao, Q. Zhou, Z. Zhang, H. Dou, L. Zhao, X. Sui, J. Cai, Y. Zhang, B. Liu, Y. Hu, A. Yu, S. Sun, Z. Wang, Z. Chen, Self-templated hierarchically porous carbon nanorods embedded with atomic Fe-N₄ active sites as efficient oxygen reduction electrocatalysts in Zn-air batteries, *Adv. Funct. Mater.* 31 (2021), 2008085, <https://doi.org/10.1002/adfm.202008085>.
- Q. Zhu, W. Xia, L. Zheng, R. Zou, Z. Liu, Q. Xu, Atomically dispersed Fe/N-doped hierarchical carbon architectures derived from a metal-organic framework composite for extremely efficient electrocatalysis, *ACS Energy Lett.* 2 (2017) 504–511, <https://doi.org/10.1021/acseenergylett.6b00686>.
- L. Guo, S. Hwang, B. Li, F. Yang, M. Wang, M. Chen, X. Yang, S.G. Karakalos, D. A. Cullen, Z. Feng, G. Wang, G. Wu, H. Xu, Promoting atomically dispersed MnN₄ sites via sulfur doping for oxygen reduction: unveiling intrinsic activity and degradation in fuel cells, *ACS Nano* 15 (2021) 6886–6899, <https://doi.org/10.1021/acsnano.0c10637>.
- M. Qiao, Y. Wang, Q. Wang, G. Hu, X. Mamat, S. Zhang, S. Wang, Hierarchically ordered porous carbon with atomically dispersed FeN₄ for ultraefficient oxygen reduction reaction in proton-exchange membrane fuel cells, *Angew. Chem. Int. Ed.* 132 (2020) 2710–2716, <https://doi.org/10.1002/ange.201914123>.
- L. Ye, G. Chai, Z. Wen, Zn-MOF-74 derived N-doped mesoporous carbon as pH-universal electrocatalyst for oxygen reduction reaction, *Adv. Funct. Mater.* 27 (2017), 1606190, <https://doi.org/10.1002/adfm.201606190>.
- K. Yuan, D. Lützenkirchen-Hecht, L. Li, L. Shuai, Y. Li, R. Cao, M. Qiu, X. Zhuang, M.K.H. Leung, Y. Chen, U. Scherf, Boosting oxygen reduction of single iron active sites via geometric and electronic engineering: nitrogen and phosphorus dual coordination, *J. Am. Chem. Soc.* 142 (2020) 2404–2412, <https://doi.org/10.1021/jacs.9b11852>.
- H. Shang, X. Zhou, J. Dong, A. Li, X. Zhao, Q. Liu, Y. Lin, J. Pei, Z. Li, Z. Jiang, D. Zhou, L. Zheng, Y. Wang, J. Zhou, Z. Yang, R. Cao, R. Sarangi, T. Sun, X. Yang, X. Zheng, W. Yan, Z. Zhuang, J. Li, W. Chen, D. Wang, J. Zhang, Y. Li, Engineering unsymmetrically coordinated Cu₃S₂N₃ single atom sites with enhanced oxygen reduction activity, *Nat. Commun.* 11 (2020) 3049, <https://doi.org/10.1038/s41467-020-16848-8>.
- Y. Chen, R. Gao, S. Ji, H. Li, K. Tang, P. Jiang, H. Hu, Z. Zhang, H. Hao, Q. Qu, X. Liang, W. Chen, J. Dong, D. Wang, Y. Li, Atomic-level modulation of electronic density at cobalt single-atom sites derived from metal-organic frameworks: enhanced oxygen reduction performance, *Angew. Chem. Int. Ed.* 60 (2021) 3212–3221, <https://doi.org/10.1002/anie.202012798>.
- X. Cheng, J. Yang, W. Yan, Y. Han, X. Qu, S. Yin, C. Chen, R. Ji, Y. Li, G. Li, G. Li, Y. Jiang, S. Sun, Nano-geometric deformation and synergistic Co nanoparticles—Co-N₄ composite sites for proton exchange membrane fuel cells, *Energy Environ. Sci.* 14 (2021) 5958–5967, <https://doi.org/10.1039/D1EE01715B>.

- [25] X. Wei, S. Song, N. Wu, X. Luo, L. Zheng, L. Jiao, H. Wang, Q. Fang, L. Hu, W. Gu, W. Song, C. Zhu, Synergistically enhanced single-atomic site Fe by Fe₃C@C for boosted oxygen reduction in neutral electrolyte, *Nano Energy* 84 (2021), 105840, <https://doi.org/10.1016/j.nanoen.2021.105840>.
- [26] H. Wang, F. Yin, N. Liu, R. Kou, X. He, C. Sun, B. Chen, D. Liu, H. Yin, Engineering Fe-Fe₃C@Fe-N-C active sites and hybrid structures from dual metal-organic frameworks for oxygen reduction reaction in H₂-O₂ fuel cell and Li-O₂ battery, *Adv. Funct. Mater.* 29 (2019), 1901531, <https://doi.org/10.1002/adfm.201901531>.
- [27] G. Chen, P. Liu, Z. Liao, F. Sun, Y. He, H. Zhong, T. Zhang, E. Zschech, M. Chen, G. Wu, J. Zhang, X. Feng, Zinc-mediated template synthesis of Fe-N-C electrocatalysts with densely accessible Fe-N_x active sites for efficient oxygen reduction, *Adv. Mater.* 32 (2020), 1907399, <https://doi.org/10.1002/adma.201907399>.
- [28] L. Gao, X. Gao, P. Jiang, C. Zhang, H. Guo, Y. Cheng, Atomically dispersed iron with densely exposed active sites as bifunctional oxygen catalysts for zinc-air flow batteries, *Small* 18 (2022), 2105892, <https://doi.org/10.1002/sml.202105892>.
- [29] W. Zhai, S. Huang, C. Lu, X. Tang, L. Li, B. Huang, T. Hu, K. Yuan, X. Zhuang, Y. Chen, Simultaneously integrate iron single atom and nanocluster triggered tandem effect for boosting oxygen electroreduction, *Small* 18 (2022), 2107225, <https://doi.org/10.1002/sml.202107225>.
- [30] X. Wan, Q. Liu, J. Liu, S. Liu, X. Liu, L. Zheng, J. Shang, R. Yu, J. Shui, Iron atom-cluster interactions increase activity and improve durability in Fe-N-C fuel cells, *Nat. Commun.* 13 (2022) 2963, <https://doi.org/10.1038/s41467-022-30702-z>.
- [31] J. Han, X. Meng, L. Lu, J. Bian, Z. Li, C. Sun, Single-atom Fe-N_x-C as an efficient electrocatalyst for zinc-air batteries, *Adv. Funct. Mater.* 29 (2019), 1808872, <https://doi.org/10.1002/adfm.201808872>.
- [32] Y. Sun, L. Silvili, N.R. Sahraie, W. Ju, J. Li, A. Zitolo, S. Li, A. Bagger, L. Arnarson, X. Wang, T. Moeller, D. Bernsmeier, J. Rossmel, F. Jaouen, P. Strasser, Activity-selectivity trends in the electrochemical production of hydrogen peroxide over single-site metal-nitrogen-carbon catalysts, *J. Am. Chem. Soc.* 141 (2019) 12372–12381, <https://doi.org/10.1021/jacs.9b05576>.
- [33] J. Han, H. Bao, J.Q. Wang, L. Zheng, S. Sun, Z.L. Wang, C. Sun, 3D N-doped ordered mesoporous carbon supported single-atom Fe-N-C catalysts with superior performance for oxygen reduction reaction and zinc-air battery, *Appl. Catal. B Environ.* 280 (2021), 119411, <https://doi.org/10.1016/j.apcatb.2020.119411>.
- [34] Y. Zhan, H. Zeng, F. Xie, H. Zhang, W. Zhang, Y. Jin, Y. Zhang, J. Chen, H. Meng, Templated growth of Fe/N/C catalyst on hierarchically porous carbon for oxygen reduction reaction in proton exchange membrane fuel cells, *J. Power Sources* 431 (2019) 31–39, <https://doi.org/10.1016/j.jpowsour.2019.05.051>.
- [35] F. Yang, Z. Liu, X. Liu, A. Feng, B. Zhang, W. Yang, Y. Li, Cobalt single atoms anchored on nitrogen-doped porous carbon as an efficient catalyst for oxidation of silanes, *Green Chem.* 23 (2021) 1026–1035, <https://doi.org/10.1039/d0gc03498c>.
- [36] C. Zhao, J. Liu, J. Wang, D. Ren, J. Yu, X. Chen, B. Li, Q. Zhang, $\Delta E = 0.63$ V bifunctional oxygen electrocatalyst enables high-rate and long-cycling zinc-air batteries, *Adv. Mater.* 33 (2021), 2008606, <https://doi.org/10.1002/adma.202008606>.
- [37] X. Zhao, P. Pachfule, S. Li, J.R.J. Simke, J. Schmidt, A. Thomas, Bifunctional electrocatalysts for overall water splitting from an iron/nickel-based bimetallic metal-organic framework/dicyandiamide composite, *Angew. Chem. Int. Ed.* 130 (2018) 9059–9064, <https://doi.org/10.1002/ange.201803136>.
- [38] X. Cui, L. Gao, S. Lei, S. Liang, J. Zhang, C.D. Sewell, W. Xue, Q. Liu, Z. Lin, Y. Yang, Simultaneously crafting single-atomic Fe sites and graphitic layer-wrapped Fe₃C nanoparticles encapsulated within mesoporous carbon tubes for oxygen reduction, *Adv. Funct. Mater.* 31 (2021), 2009197, <https://doi.org/10.1002/adfm.202009197>.
- [39] Y. He, Y. Li, J. Zhang, S. Wang, D. Huang, G. Yang, X. Yi, H. Lin, X. Han, W. Hu, Y. Deng, J. Ye, Low-temperature strategy toward Ni-NC@Ni core-shell nanostructure with single-Ni sites for efficient CO₂ electroreduction, *Nano Energy* 77 (2020), 105010, <https://doi.org/10.1016/j.nanoen.2020.105010>.
- [40] X. Wan, X. Liu, Y. Li, R. Yu, L. Zheng, W. Yan, H. Wang, M. Xu, J. Shui, Fe-N-C electrocatalyst with dense active sites and efficient mass transport for high-performance proton exchange membrane fuel cells, *Nat. Catal.* 2 (2019) 259–268, <https://doi.org/10.1038/s41929-019-0237-3>.
- [41] Y. Yao, H. Chen, C. Lian, F. Wei, D. Zhang, G. Wu, B. Chen, S. Wang, Fe, Co, Ni nanocrystals encapsulated in nitrogen-doped carbon nanotubes as Fenton-like catalysts for organic pollutant removal, *J. Hazard. Mater.* 314 (2016) 129–139, <https://doi.org/10.1016/j.jhazmat.2016.03.089>.
- [42] K. Fu, Y. Wang, L. Mao, X. Yang, J. Jin, S. Yang, G. Li, Strongly coupled Co, N doped carbon nanotubes/graphene-like carbon nanosheets as efficient oxygen reduction electrocatalysts for primary Zinc-air battery, *Chem. Eng. J.* 351 (2018) 94–102, <https://doi.org/10.1016/j.cej.2018.06.059>.
- [43] F. Ma, K. Srinivas, X. Zhang, Z. Zhang, Y. Wu, D. Liu, W. Zhang, Q. Wu, Y. Chen, Mo₂N quantum dots decorated N-doped graphene nanosheets as dual-functional interlayer for dendrite-free and shuttle-free lithium-sulfur batteries, *Adv. Funct. Mater.* 32 (2022), 2206113, <https://doi.org/10.1002/adfm.202206113>.
- [44] F. Ma, B. Yu, X. Zhang, Z. Zhang, K. Srinivas, X. Wang, D. Liu, B. Wang, W. Zhang, Q. Wu, Y. Chen, WN_{0.67}-embedded N-doped graphene-nanosheet interlayer as efficient polysulfide catalyst and absorbant for high-performance lithium-sulfur batteries, *Chem. Eng. J.* 431 (2022), 133439, <https://doi.org/10.1016/j.cej.2021.133439>.
- [45] K. Srinivas, F. Ma, Y. Liu, Z. Zhang, Y. Wu, Y. Chen, Metal-organic framework-derived Fe-doped Ni₃Se₄/NiSe₂ heterostructure-embedded mesoporous tubes for boosting oxygen evolution reaction, *ACS Appl. Mater. Interfaces* 14 (2022) 52927–52939, <https://doi.org/10.1021/acsami.2c16133>.
- [46] Y. Jiang, L. Yang, T. Sun, J. Zhao, Z. Lyu, O. Zhuo, X. Wang, Q. Wu, J. Ma, Z. Hu, Significant contribution of intrinsic carbon defects to oxygen reduction activity, *ACS Catal.* 5 (2015) 6707–6712, <https://doi.org/10.1021/acscatal.5b01835>.
- [47] Y. Jia, L. Zhang, L. Zhuang, H. Liu, X. Yan, X. Wang, J. Liu, J. Wang, Y. Zheng, Z. Xiao, E. Taran, J. Chen, D. Yang, Z. Zhu, S. Wang, L. Dai, X. Yao, Identification of active sites for acidic oxygen reduction on carbon catalysts with and without nitrogen doping, *Nat. Catal.* 2 (2019) 688–695, <https://doi.org/10.1038/s41929-019-0297-4>.
- [48] J. Sheng, S. Sun, G. Jia, S. Zhu, Y. Li, Doping effect on mesoporous carbon-supported single-site bifunctional catalyst for zinc-air batteries, *ACS Nano* 16 (2022) 15994–16002, <https://doi.org/10.1021/acsnano.2c03565>.
- [49] M. Cao, Y. Liu, K. Sun, H. Li, X. Lin, P. Zhang, L. Zhou, A. Wang, S. Mehdi, X. Wu, J. Jiang, B. Li, Coupling Fe₃C nanoparticles and N-doping on wood-derived carbon to construct reversible cathode for Zn-air batteries, *Small* 18 (2022), 2202014, <https://doi.org/10.1002/sml.202202014>.
- [50] K. Srinivas, Y. Chen, B. Wang, B. Yu, Y. Lu, Z. Su, W. Zhang, D. Yang, Metal-organic framework-derived Fe-doped Ni₃Fe/NiFe₂O₄ heteronanoparticle-decorated carbon nanotube network as a highly efficient and durable bifunctional electrocatalyst, *ACS Appl. Mater. Interfaces* 12 (2020) 55782–55794, <https://doi.org/10.1021/acsami.0c13836>.
- [51] K. Srinivas, Y. Chen, B. Wang, B. Yu, X. Wang, Y. Hu, Y. Lu, W. Li, W. Zhang, D. Yang, Metal-organic framework-derived NiS/Fe₃O₄ heterostructure-decorated carbon nanotubes as highly efficient and durable electrocatalysts for oxygen evolution reaction, *ACS Appl. Mater. Interfaces* 12 (2020) 31552–31563, <https://doi.org/10.1021/acsami.0c09737>.
- [52] K. Srinivas, X. Chen, D. Liu, F. Ma, X. Zhang, W. Zhang, H. Lin, Y. Chen, Surface modification of metal-organic frameworks under sublimated iron-atmosphere by controlled carbonization for boosted oxygen evolution reaction, *Nano Res.* 15 (2022) 5884–5894, <https://doi.org/10.1007/s12274-022-4231-8>.
- [53] F. Kong, Y. Huang, M. Chen, G. Meng, H. Tian, Y. Chen, Z. Chang, C. Chen, W. Sun, X. Cui, J. Shi, Creation of densely exposed and cavity-edged single Fe active sites for enhanced oxygen electroreduction, *Appl. Catal. B Environ.* 317 (2022), 121768, <https://doi.org/10.1016/j.apcatb.2022.121768>.
- [54] K. Srinivas, Y. Chen, Z. Su, B. Yu, M. Karpuraranjith, F. Ma, X. Wang, W. Zhang, D. Yang, Heterostructural CoFe₂O₄/CoO nanoparticles-embedded carbon nanotubes network for boosted overall water-splitting performance, *Electrochim. Acta* 404 (2022), 139745, <https://doi.org/10.1016/j.electacta.2021.139745>.
- [55] J. Zhu, Y. Huang, W. Mei, C. Zhao, C. Zhang, J. Zhang, I.S. Amiin, S. Mu, Effects of intrinsic pentagon defects on electrochemical reactivity of carbon nanomaterials, *Angew. Chem. Int. Ed.* 131 (2019) 3899–3904, <https://doi.org/10.1002/ange.201813805>.
- [56] M. Jiang, F. Wang, F. Yang, H. He, J. Yang, W. Zhang, J. Luo, J. Zhang, C. Fu, Rationalization on high-loading iron and cobalt dual metal single atoms and mechanistic insight into the oxygen reduction reaction, *Nano Energy* 93 (2022), 106793, <https://doi.org/10.1016/j.nanoen.2021.106793>.
- [57] D. Liu, K. Srinivas, X. Chen, F. Ma, X. Zhang, X. Wang, B. Wang, Y. Chen, Dual Fe, Zn single atoms anchored on carbon nanotubes inlaid N, S-doped hollow carbon polyhedrons for boosting oxygen reduction reaction, *J. Colloid Interface Sci.* 624 (2022) 680–690, <https://doi.org/10.1016/j.jcis.2022.05.167>.
- [58] C. Xu, C. Guo, J. Liu, B. Hu, J. Dai, M. Wang, R. Jin, Z. Luo, H. Li, C. Chen, Accelerating the oxygen adsorption kinetics to regulate the oxygen reduction catalysis via Fe₃C nanoparticles coupled with single Fe-N₄ sites, *Energy Storage Mater.* 51 (2022) 149–158, <https://doi.org/10.1016/j.ensm.2022.06.038>.
- [59] F. Zhou, P. Yu, F. Sun, G. Zhang, X. Liu, L. Wang, The cooperation of Fe₃C nanoparticles with isolated single iron atoms to boost the oxygen reduction reaction for Zn-air batteries, *J. Mater. Chem. A* 9 (2021) 6831–6840, <https://doi.org/10.1039/d1ta00039j>.
- [60] X. Xiang, X. Zhang, B. Yan, K. Wang, Y. Wang, D. Lyu, S. Xi, Z. Qun Tian, P. Kang Shen, Atomic iron coordinated by nitrogen doped carbon nanoparticles synthesized via a synchronous complexation-polymerization strategy as efficient oxygen reduction reaction electrocatalysts for zinc-air battery and fuel cell application, *Chem. Eng. J.* 440 (2022), 135721, <https://doi.org/10.1016/j.cej.2022.135721>.
- [61] X. Wang, H. Xiao, A. Li, Z. Li, S. Liu, Q. Zhang, Y. Gong, L. Zheng, Y. Zhu, C. Chen, D. Wang, Q. Peng, L. Gu, X. Han, J. Li, Y. Li, Constructing NiCo/Fe₃O₄ heteroparticles within MOF-74 for efficient oxygen evolution reactions, *J. Am. Chem. Soc.* 140 (2018) 15336–15341, <https://doi.org/10.1021/jacs.8b08744>.
- [62] Z. Wang, X. Jin, C. Zhu, Y. Liu, H. Tan, R. Ku, Y. Zhang, L. Zhou, Z. Liu, S. Hwang, H.J. Fan, Atomically dispersed Co₂-N₆ and Fe-N₄ costructures boost oxygen reduction reaction in both alkaline and acidic media, *Adv. Mater.* 33 (2021), 2104718, <https://doi.org/10.1002/adma.202104718>.
- [63] W.-J. Jiang, L. Gu, L. Li, Y. Zhang, X. Zhang, L.-J. Zhang, J.-Q. Wang, J.-S. Hu, Z. Wei, L.-J. Wan, Understanding the high activity of Fe-N-C electrocatalysts in oxygen reduction: Fe/Fe₃C nanoparticles boost the activity of Fe-N_x, *J. Am. Chem. Soc.* 138 (2016) 3570–3578, <https://doi.org/10.1021/jacs.6b00757>.
- [64] B. Wang, K. Srinivas, Y. Liu, D. Liu, X. Zhang, W. Zhang, Y. Chen, N-doped CNTs capped with carbon layer armored CoFe alloy as highly stable bifunctional catalyst for oxygen electrocatalysis, *Nano Res.* 15 (2022) 3971–3979, <https://doi.org/10.1007/s12274-022-4084-1>.
- [65] H. Jin, R. Yu, C. Hu, P. Ji, Q. Ma, B. Liu, D. He, S. Mu, Size-controlled engineering of cobalt metal catalysts through a coordination effect for oxygen electrocatalysis, *Appl. Catal. B Environ.* 317 (2022), 121766, <https://doi.org/10.1016/j.apcatb.2022.121766>.
- [66] K. Srinivas, Y. Chen, X. Wang, B. Wang, M. Karpuraranjith, W. Wang, Z. Su, W. Zhang, D. Yang, Constructing Ni/NiS heteronanoparticle-embedded metal-organic framework-derived nanosheets for enhanced water-splitting

- catalysis, *ACS Sustain. Chem. Eng.* 9 (2021) 1920–1931, <https://doi.org/10.1021/acssuschemeng.0c08543>.
- [67] K. Srinivas, Y. Lu, Y. Chen, W. Zhang, D. Yang, FeNi₃-Fe₃O₄ heterogeneous nanoparticles anchored on 2D MOF nanosheets/1D CNT matrix as highly efficient bifunctional electrocatalysts for water splitting, *ACS Sustain. Chem. Eng.* 8 (2020) 3820–3831, <https://doi.org/10.1021/acssuschemeng.9b07182>.
- [68] C.-X. Zhao, J.-N. Liu, J. Wang, D. Ren, B.-Q. Li, Q. Zhang, Recent advances of noble-metal-free bifunctional oxygen reduction and evolution electrocatalysts, *Chem. Soc. Rev.* 50 (2021) 7745–7778, <https://doi.org/10.1039/D1CS00135C>.
- [69] L. Zhong, C. Jiang, M. Zheng, X. Peng, T. Liu, S. Xi, X. Chi, Q. Zhang, L. Gu, S. Zhang, G. Shi, L. Zhang, K. Wu, Z. Chen, T. Li, M. Dahbi, J. Alami, K. Amine, J. Lu, Wood carbon based single-atom catalyst for rechargeable Zn–air batteries, *ACS Energy Lett.* 6 (2021) 3624–3633, <https://doi.org/10.1021/acsenergylett.1c01678>.
- [70] X. Yang, X. Zheng, H. Li, B. Luo, Y. He, Y. Yao, H. Zhou, Z. Yan, Y. Kuang, Z. Huang, Non-noble-metal catalyst and Zn/graphene film for low-cost and ultra-long-durability solid-state Zn–air batteries in harsh electrolytes, *Adv. Funct. Mater.* 32 (2022), 2200397, <https://doi.org/10.1002/adfm.202200397>.
- [71] Y. Sun, Y. Li, S. You, X. Li, Y. Zhang, Z. Cai, M. Liu, N. Ren, J. Zou, Fe₃C/CoFe₂O₄ nanoparticles wrapped in one-dimensional MIL-53(Fe)-derived carbon nanofibers as efficient dual-function oxygen catalysts, *Chem. Eng. J.* 424 (2021), 130460, <https://doi.org/10.1016/j.cej.2021.130460>.
- [72] J.-S. Lee, S. Tai Kim, R. Cao, N.-S. Choi, M. Liu, K.T. Lee, J. Cho, Metal–air batteries with high energy density: li–air versus Zn–air, *Adv. Energy Mater.* 1 (2011) 34–50, <https://doi.org/10.1002/aenm.201000010>.
- [73] G.W. Heise, Air Depolarized Primary Battery, U.S. Pat. (1933) 1899615.
- [74] D. Linden, T.B. Reddy, *Handbooks of Batteries*, McGraw-Hill, 2001.
- [75] F.P. Veltz, Medical systems, devices and methods, U.S. Pat. 2017. 0173262.
- [76] L. Jörissen, Bifunctional oxygen/air electrodes, *J. Power Sources* 155 (2006) 23–32, <https://doi.org/10.1016/j.jpowsour.2005.07.038>.
- [77] V. Neburchilov, H. Wang, J.J. Martin, W. Qu, A review on air cathodes for zinc–air fuel cells, *J. Power Sources* 195 (2010) 1271–1291, <https://doi.org/10.1016/j.jpowsour.2009.08.100>.
- [78] P. Chen, K. Zhang, D. Tang, W. Liu, F. Meng, Q. Huang, J. Liu, Recent progress in electrolytes for Zn–air batteries, *Front. Chem.* 8 (2020) 00372, <https://doi.org/10.3389/fchem.2020.00372>.
- [79] S.F.M. Qi, and T. Zawodzinski, Reversible bifunctional air electrode catalyst for rechargeable metal air battery and regenerative fuel cell, U.S. Pat. (2021) 11031606.
- [80] E.S. Buzzelli, Metal/air cells and improved air electrodes for use thereon, US Pat. (1976) 3977901.
- [81] J. Chottiner, Multi-ply laminar pasted air electrodes, US Pat. (1979) 4152489.
- [82] J.F. Jackovitz and C.-T. Liu, Bifunctional gas diffusion electrodes employing wettable, non-wettable layered structure using the mud-cake concept, US Pat. (1984) 5318862.
- [83] N.Y.S. Yokoyama, and S. Yamamoto, Battery using layered double hydroxide, U.S. Pat. (2010) 10700385.
- [84] Z. Chen and Z. Chen, Core-shell structured bifunctional catalysts for metal air battery/fuel cell, U.S. Pat. (2017) 9590253.
- [85] Y. Wang, F. Chu, J. Zeng, Q. Wang, T. Naren, Y. Li, Y. Cheng, Y. Lei, F. Wu, Single atom catalysts for fuel cells and rechargeable batteries: principles, advances, and opportunities, *ACS Nano* 15 (2021) 210–239, <https://doi.org/10.1021/acsnano.0c08652>.
- [86] L. Peng, J. Yang, Y. Yang, F. Qian, Q. Wang, D. Sun-Waterhouse, L. Shang, T. Zhang, G.I.N. Waterhouse, Mesopore-rich Fe–N–C catalyst with FeN₄–O–NC single-atom sites delivers remarkable oxygen reduction reaction performance in alkaline media, *Adv. Mater.* 34 (2022), 2202544, <https://doi.org/10.1002/adma.202202544>.
- [87] X. Han, G. He, Y. He, J. Zhang, X. Zheng, L. Li, C. Zhong, W. Hu, Y. Deng, T. Ma, Engineering catalytic active sites on cobalt oxide surface for enhanced oxygen electrocatalysis, *Adv. Energy Mater.* 8 (2018), 1702222, <https://doi.org/10.1002/aenm.201702222>.